

Christoph Baumann

X-ray Transmission of Radiators
for the ALICE-TRD

— 2005 —

EXPERIMENTELLE PHYSIK

X-ray Transmission of Radiators
for the ALICE-TRD

Diplomarbeit

von

Christoph Baumann

Westfälische Wilhelms-Universität Münster

Institut für Kernphysik

— Februar 2005 —

Contents

| | | |
|-------|--|----|
| 1 | Introduction | 5 |
| 2 | ALICE and the LHC | 7 |
| 2.1 | The Large Hadron Collider | 7 |
| 2.2 | The ALICE Experiment | 9 |
| 2.2.1 | Goals of ALICE | 9 |
| 2.2.2 | Setup of ALICE | 11 |
| 3 | The ALICE Transition Radiation Detector | 15 |
| 3.1 | Theoretical Background of Transition Radiation | 15 |
| 3.2 | Design Considerations | 17 |
| 3.2.1 | Performance Issues | 18 |
| 3.2.2 | Setup of the ALICE-TRD | 19 |
| 4 | Theoretical Background on X-rays | 25 |
| 4.1 | Generation of X-rays | 25 |
| 4.2 | Attenuation of X-rays in Matter | 26 |
| 4.3 | Measuring X-rays | 27 |
| 5 | Experimental Setup | 31 |
| 5.1 | Motivation and Tasks | 31 |
| 5.2 | Overview | 31 |
| 5.3 | Test Stand | 32 |
| 5.3.1 | The X-ray Generator | 33 |
| 5.3.2 | The Si(Li) Detector | 34 |
| 5.4 | Data Acquisition and Control | 35 |

| | | |
|-------|---|----|
| 5.4.1 | Aptec MCard System | 35 |
| 5.4.2 | Labview System | 35 |
| 5.5 | Calibration of the Setup | 39 |
| 5.5.1 | Energy Calibration | 39 |
| 5.5.2 | Energy Resolution | 40 |
| 5.5.3 | Determination of the Dead Time | 41 |
| 5.6 | Offline Analysis | 43 |
| 6 | Quality Control Measurements and Analysis | 47 |
| 6.1 | X-Ray Transmission of the Components | 47 |
| 6.1.1 | Cover Plates | 47 |
| 6.1.2 | Bars | 51 |
| 6.1.3 | Polypropylene Mats | 51 |
| 6.2 | X-ray Transmission of the Full Radiator | 52 |
| 6.3 | Results | 54 |
| 7 | Parameterization of the Transmission Function | 59 |
| 7.1 | Parameterization of X-Ray Transmission | 59 |
| 7.2 | Mats | 61 |
| 7.3 | Rohacell HF71 | 61 |
| 7.4 | Cover Plates | 62 |
| 7.5 | Full Radiator | 64 |
| 7.6 | Influence of the Transmission on the Gas Gain | 66 |
| 8 | Summary | 69 |
| A | Data Tables | 71 |
| | Bibliography | 85 |
| | Danksagung | 89 |

1. Introduction

In 2007 the new Large Hadron Collider (LHC) is scheduled to start its operation at CERN¹, Geneva. It will permit the exploration of previously inaccessible ranges of particle energy. ALICE (*A Large Ion Collider Experiment*) is one of five dedicated experiments at the LHC and the only one specifically designed for examining heavy ion interactions. One of the most prominent phenomena that can possibly be examined with ALICE, is certainly the Quark Gluon plasma (QGP). An important signature of the QGP are electrons produced in its early phase. To improve the separation of electrons from the pion background is the primary task of the Transition Radiation Detector (TRD), which essentially consists of two parts: The radiator and the drift chamber. While ultrarelativistic electrons produce so-called transition radiation, with a distribution peaked at approximately 10 keV in the radiator, pions do not.

The transition radiation is detected in the drift chamber of the TRD together with the corresponding particle, the information derived from the TR helps to improve the separation between electrons and pions.

The yield of transition radiation photons from the radiator has been optimized in the design process of the TRD. An important limitation of the yield is the attenuation of photons within the radiator. Prototype tests have shown that the attenuation in various components can vary significantly. The exact energy dependent attenuation of the components and the full radiators has not been measured so far.

In this diploma thesis systematic quantitative tests of the photon transmission properties of the radiators produced at the *Institut für Kernphysik* in Münster will be described, with a focus on the variation of the transmission properties of different radiators. In addition, an energy dependent parametrization of the transmission function will be presented. These measurements are an essential part of the quality control for the mass production of the radiators.

¹European Organization for Nuclear Research

2. ALICE and the LHC

2.1 The Large Hadron Collider

The LHC, which is currently under construction at CERN, will offer energy ranges previously not available in proton-proton and heavy ion collisions. It is under construction inside the 27 km long tunnel previously used for the LEP¹(see Figure 2.1). It is designed for proton-proton collisions with center-of-mass energies of up to 14 TeV and a peak luminosity of $10^{34}\text{cm}^{-2}\text{s}^{-1}$. For collisions of Pb-ions the maximum center-of-mass energy will be 1150 TeV at a luminosity of $10^{27}\text{cm}^{-2}\text{s}^{-2}$ [LHC95].

At these energies, a great variety of new physical phenomena is expected, some of the most prominent are presented here briefly.

One aim is the production of the Higgs-Boson and the measurement of its mass m_H . Assuming an elementary Higgs particle, measurements suggest an upper limit for m_H of 200 GeV. In 2000, experiments at LEP have yielded a lower limit $m_H > 114$ GeV [Ell04]. If such a Higgs particle predicted by the Standard Model does not exist it will be possible to check other explanations, as for example Higgs particles proposed by supersymmetric models. It will also be possible to search for other particles predicted by these models [Wom97].

B-physics will be another important field of research as the production cross section for $b\bar{b}$ pairs will significantly exceed cross sections available at other facilities [Tar02]. Therefore high precision measurements of the CP violation in the b -quark system will be possible.

Especially important for this thesis are collisions of Pb-ions at LHC energies. It is expected that a very dense and hot state of matter is formed in the course of the reaction. Results from SPS and RHIC [Lud03] provide evidence that it will be possible at the LHC to produce the theoretically predicted Quark-Gluon Plasma (QGP) and examine it in detail [BM99].

Other lines of investigation include the search for particles and resonances predicted by superstring theories or by technicolor models of electroweak symmetry breaking [Ell04, Wom97].

¹Large Electron Positron Collider

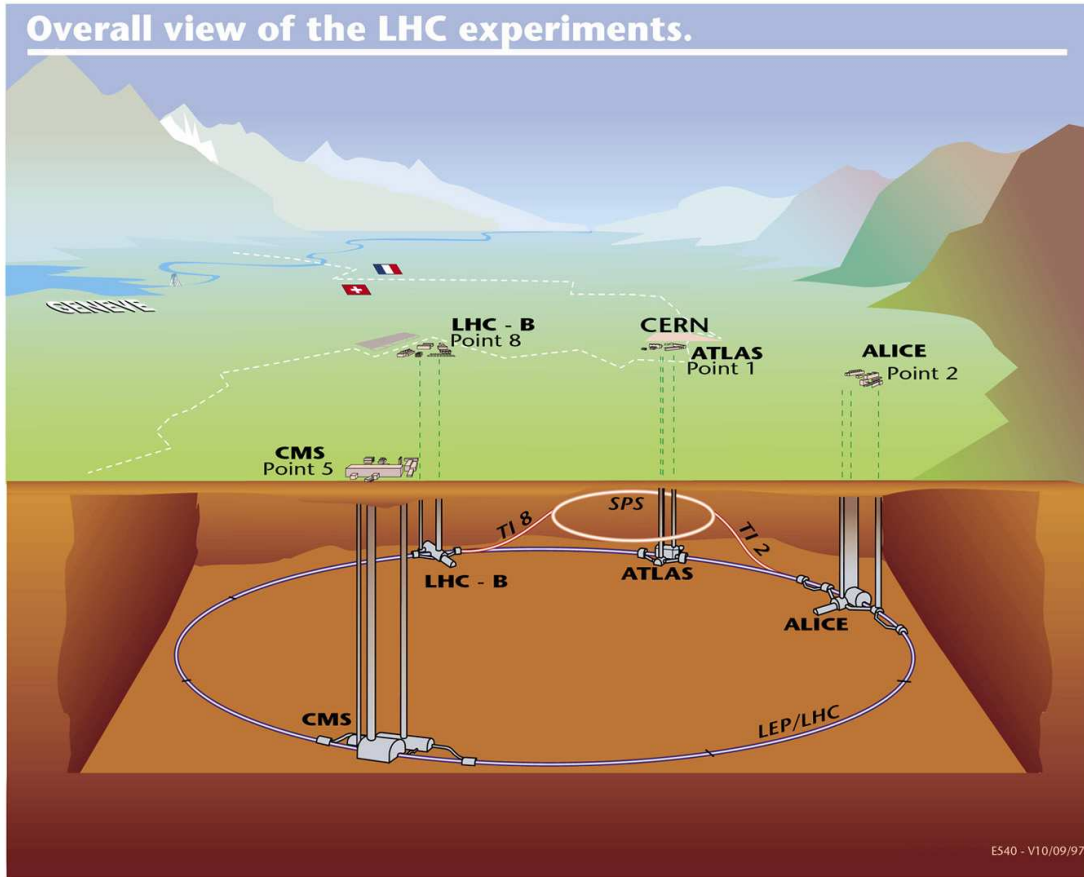


Figure 2.1: View of the LHC and its experiments [CER99]

The physics program will be covered by five experiments: ATLAS², CMS³, LHCb⁴, ALICE and TOTEM⁵. The two largest, ATLAS and CMS, will focus on the measurement of the Higgs-boson and of particles predicted by theories extending or replacing the Standard Model [Pai02]. Also B-physics will be possible with both experiments to some extent. At least CMS will also be used for Pb+Pb collisions due to its high sensitivity in the high p_t ⁶ regime [Tar02]. The LHCb experiment is specif-

²A Toroidal LHC Apparatus

³Compact Muon Solenoid

⁴The Large Hadron Collider beauty Experiment

⁵Total and Elastic Measurement

⁶In accelerator physics, the momentum of particle is often divided into the longitudinal momentum p_L along the beam axis and the transverse momentum p_T , which is orthogonal to the beam axis. With p being the absolute value of the momentum of the particle and ν being the

ically designed for B-physics and will focus on the measurement of the CP violation. TOTEM is a very small experiment, which will be integrated in the setup of CMS and which is specifically designed to measure the p+p cross-section [Ava03]. The design of ALICE has been optimized for the measurement of heavy ion interactions and will be detailed in the following chapter.

2.2 The ALICE Experiment

'My NAME is Alice, but—'

'It's a stupid enough name!' Humpty Dumpty interrupted impatiently.

'What does it mean?'

'MUST a name mean something?' Alice asked doubtfully.

'Of course it must,' Humpty Dumpty said with a short laugh[.]

- *Lewis Carrol, 'Through the Looking-Glass'*

ALICE⁷ has been designed for the examination of heavy ion collisions at the LHC. With its high granularity detectors particles produced in an ultrarelativistic heavy ion collision can be identified with large acceptance [ALI95].

2.2.1 Goals of ALICE

Experiments at SPS and RHIC have already observed an extremely hot and dense state of matter which carries many traits of the QGP.

With the higher regions of energy available at LHC this state is predicted to exist for longer periods of time and over larger space. Predictions for the lifetime τ_{QGP} of the possible QGP at the different colliders suggest that at LHC the QGP lifetimes will exceed the previously available ones by about one order of magnitude. With $\tau_{\text{QGP}} \approx 4.5 - 12 \text{ fm}/c$ the expected lifetime is also large compared to the formation time $\tau_0 \ll 1 \text{ fm}/c$ [Sch02], thus the impact of initial state effects on the data is reduced. It is therefore expected that a detailed search for a great variety of theoretically predicted signatures of the QGP will be possible [And04, Sch02]. Various authors have discussed signatures of the QGP which are relevant for ALICE (e.g. [Ale02, Sch02, Pai02]):

angle between the beam axis and the trajectory of the particle, these two momenta are defined by $p_T = p \cdot \sin \nu$ and $p_L = p \cos \nu$.

⁷A Large Heavy Ion Collider Experiment

A prominent signature is suppression of the bound states of the heavy b and c quarks (*quarkonia*), especially of the J/Ψ and Υ states. Due to the high quark densities within the QGP these resonances, which are produced in early hard scattering processes, are expected to be suppressed by color screening in the medium compared to open charm and beauty production. Especially the Υ is expected to be a good signature, while the suppression of the J/Ψ might be compensated for by the hadronization of $c\bar{c}$ -pairs into J/Ψ , which will be produced statistically, when the temperature of the QGP is of the order of magnitude of the charm-quark mass. Calculations show that there could be even an enhancement in the J/Ψ production due to these thermally produced quarks [BM00]. The Drell-Yan⁸ continuum will most likely not be applicable as normalization for the J/Ψ spectra at LHC energies [BM99]. Instead the production cross sections for open charm and beauty will be taken as a reference. Another important reason for the measurement of these cross sections is that secondary J/Ψ produced in the decay of B-mesons or the annihilation of a D and a \bar{D} -meson, which could possibly obscure a possible suppression of the primary J/Ψ production, can be identified. Due to the thermal $c\bar{c}$ production, an enhancement in open charm is also expected, which can be quantified on the basis of the production cross section measurements.

Jet quenching, the suppression of particle jets due to parton energy loss in the dense medium, is also able to deliver information on the earlier stages of the QGP. The energy distribution of jets from A+A collisions can be compared to appropriately scaled results from p+p measurements to quantify the energy loss. Moreover, the measurement of back-to-back correlations of jets is another tool to extract information on the medium that causes the energy loss.

So-called thermal direct photons, which are produced early in the lifetime of the QGP, can serve as another probe. These have to be separated from the large decay photon background in an ultrarelativistic nucleus-nucleus collision that will mainly be produced by decays of π^0 -particles.

In order to probe the properties of a possibly produced QGP, ALICE will, for example, allow measurements of the elliptic flow of non-central collisions and it will be possible to apply HBT analysis in order to determine the size of the deconfinement-region [Giu01].

⁸The Drell-Yan process describes the production of a lepton pair by the annihilation of a quark and an antiquark from two interacting hadrons [Won94].

The high energies at LHC will also facilitate event-by-event analysis of particles, which could formerly not be produced with the necessary multiplicity.

Besides exploring the properties of the QGP, ALICE will be able to contribute to the physics of p+p collisions due to its sensitivity at low p_T compared to ATLAS and CMS .

2.2.2 Setup of ALICE

The ALICE experiment is located in the experimental area P2, formerly occupied by the LEP experiment L3. The central part of the experiment is placed within the L3 magnet, which creates a magnetic field of 0.2 – 0.5 T, necessary for a good separation of charged particles at high p_T . [Giu02]

ALICE consists of a number of subsystems (see Figure 2.2): The Inner Tracking System (ITS), a Time Projection Chamber (TPC), a Transition Radiation Detector (TRD), a Time Of Flight Chamber (TOF), a High Momentum Particle Identification Detector (HMPID), and a Photon Spectrometer (PHOS). All of the systems mentioned so far make up the central barrel located within the L3 magnet. A muon spectrometer is placed behind a large dipole magnet and muon filters in forward direction. For small angles there are several small forward detectors (ZDC, PMD, FMD, CASTOR, T0, V0) utilized for the measurement of global properties like the impact parameter or to generate trigger events [Giu02, Sch02].

The ITS is used as tracking system together with the TPC and the TRD. It consists of six layers of silicon detectors, incorporating 3 different designs to optimize the resolution of the primary vertex. This design also permits to use the ITS as spectrometer for low p_T particles [Giu04]. It also improves the momentum resolution of high p_T particles and enables the reconstruction of secondary vertices of charmed meson and hyperon decays as well as a measurement of the primary vertex.

The TPC plays an important role within the ALICE experiment. It is used for track finding and momentum measurements, both needed for particle identification, by measuring dE/dx . Its size is determined by the maximum hit density and the length needed for a dE/dx resolution better than 10 %, yielding an inner radius of 90 cm and an outer radius of 250 cm. The length in beam direction is 500 cm. It consists of a large field cage, filled with a Ne/CO₂ gas mixture, and a highly uniform electric field created by high voltages of up to 100 kV. Multiwire proportional chambers serve as readout chambers [Del00].

The TRD has been proposed for ALICE in 1999 [TRD99] to improve the separation of electrons and pions. As the radiators of the TRD are the main focus of this thesis, the TRD and its functionality will be reviewed in more detail in Chapter 3.

The main task of the TOF is particle identification. It consists of Multigap Resistive Plate Chambers (MRPC), gaseous detectors with multiple resistive plates, which are transparent for avalanches but which prevent spark breakdowns. The TOF offers particle identification for π , K and p up to 2.5 GeV/ c [Cor02].

The HMPID has been specifically designed for high p_t particle identification. It consists of Ring Imaging Cherenkov (RICH) detectors with a C_6F_{14} fluid radiator. It will cover $\approx 15\%$ of the central barrel acceptance. The π/K identification is possible up to ≈ 3 GeV, the K/p identification up to ≈ 5 GeV.

The PHOS is located below the central barrel. It is an electromagnetic calorimeter made of $PbWO_4$. Its 17280 crystals will cover an area of $\approx 8\text{m}^2$, which corresponds to a pseudorapidity⁹ range of $-0.12 < \eta < 0.12$ [PHO99]. Its task is to detect photons from π^0 and η decays as well as directly produced photons.

Muons are tracked via the muon spectrometer arm. It consists of a composite absorber one meter behind the vertex, which has been designed to stop the majority of hadrons, photons and electrons, followed by a dipole magnet, accepting muons at angles smaller than 9° with respect to the beam axis. An absorber excludes particles at angles below 2° so that the muon arm is shielded from non-colliding Pb nuclei. The muons are tracked by ten multiwire chambers grouped in pairs. Another two tracking planes, which are placed behind a muon absorber behind the ten-plane-stack, are used for muon identification and triggering.

By utilizing these different detection techniques, ALICE will permit to explore the physics of heavy ion interactions at the unprecedented LHC beam energies.

⁹The pseudorapidity η can be used to describe the kinematic condition of a particle. It is defined via the angle θ with respect to the beam axis: $\eta = -\ln(\tan(\theta/2))$.

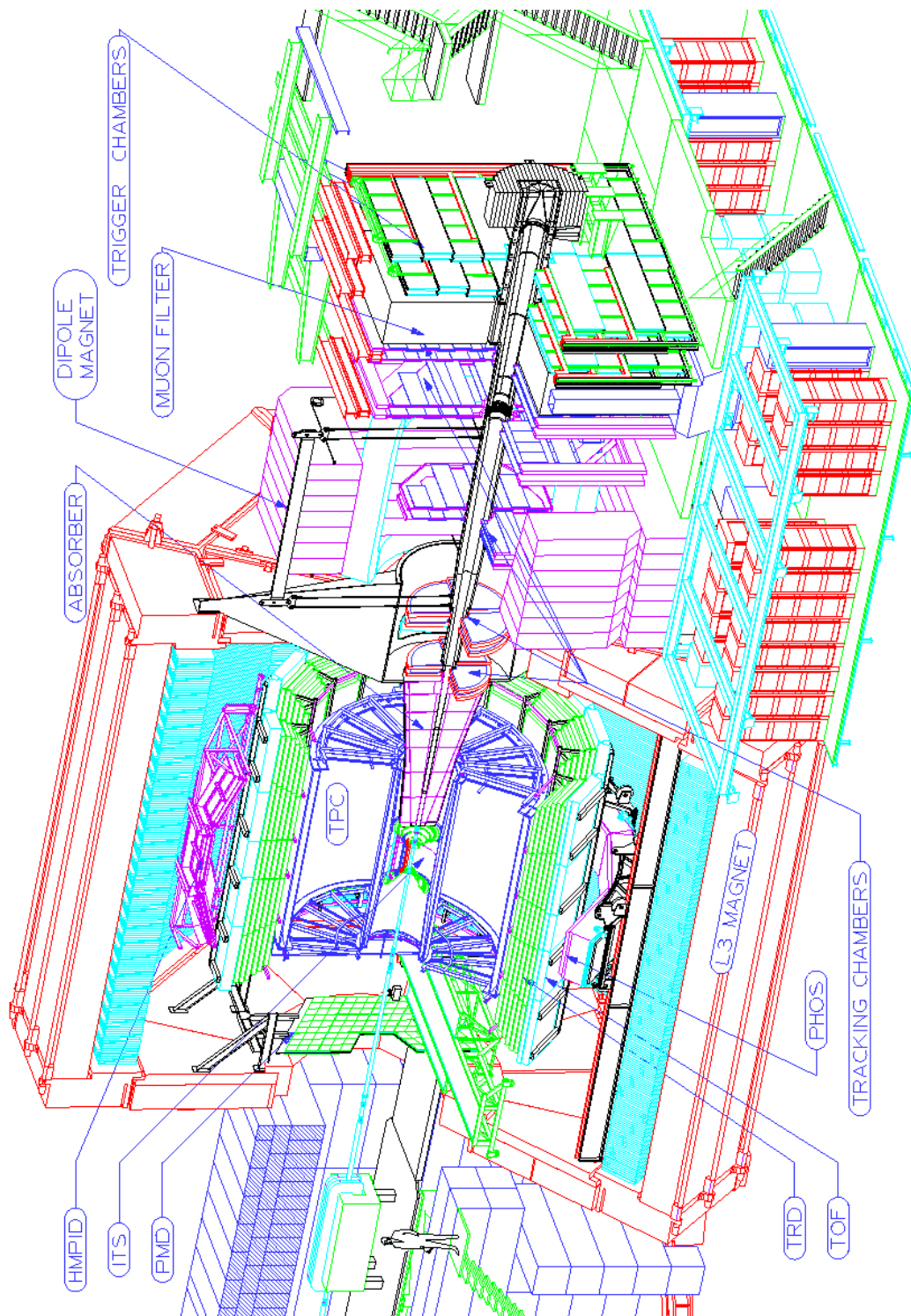


Figure 2.2: Schematic of the ALICE setup [TRD05]

3. The ALICE Transition Radiation Detector

The identification of particles over a broad energy range is obviously an essential part in a heavy-ion experiment. In order to improve the separation of pions, which are produced abundantly in a heavy ion collision, and electrons, the TRD was introduced into the design of ALICE in 1999 [TRD99]. It will improve the pion rejection, which is possible with the TPC and TOF, to a rejection factor of 100 for electrons with $p_t > 3\text{GeV}/c$.

3.1 Theoretical Background of Transition Radiation

Transition Radiation (TR) is produced by a charged particle moving at constant velocity through a medium with a non-uniform dielectric constant.

The TR was predicted in 1945 by Ginzburg and Frank [Gin45] in the optical spectrum. But due to the low intensity of optical transition radiation and the high absorption within solids, applications developed only after Garibian [Gar58, Gar60] showed that ultrarelativistic particles produce TR within the X-Ray energy range. Many properties, as for example the shape of the intensity distribution as well as the intensity itself, that were described by Ginzburg and Frank, are still valid for TR in the X-ray spectrum.

Solving the Maxwell equations for a particle moving along the z-axis from $-\infty$ to $+\infty$ through two media with different dielectric constants and an interface in the $x - y$ plane at $z = 0$ and applying a Fourier integral yields a solution, where the continuity condition is not satisfied at $z = 0$. To fulfill this condition it is necessary to add a homogenous solution of the Maxwell equations for each medium. A full derivation can be found in [Gar58]. It is shown that one can derive a single formula which explains the emission of Cherenkov radiation within each medium as well as the transmission radiation emitted at the border between the two media.

For the case of a transition from a medium with a dielectric constant $\epsilon \neq 1$ to vacuum Garibian derived the formula

$$\frac{dW}{d\Omega} = \frac{c \cdot e^2 \sin^2 \theta \cos^2 \theta}{\pi^2 v^2} \frac{\beta}{(1 - \beta^2 \cos^2 \theta)^2} \times \int_0^\infty \left| \frac{(\epsilon - 1)(1 - \beta^2 - \beta \sqrt{\epsilon - \sin^2 \theta})}{(\epsilon \cos \theta + \sqrt{\epsilon - \sin^2 \theta})(1 - \beta \sqrt{\epsilon - \sin^2 \theta})} \right|^2 d\omega \quad (3.1)$$

which gives the total amount dW of transition radiation emitted during the time of flight of the particle within the solid angle $d\Omega$. θ describes the angle of the particle trajectory relative to the surface of the material, β is defined as v/c with v being the velocity of the particle.

For ultrarelativistic particles TR is emitted with a distinct maximum at small angles. This results from the approximation of the denominator in the first term $1 - \beta^2 \cos^2 \theta = 1 - (1 - \gamma^{-2}) \cos^2 \theta \approx \gamma^{-2} + \theta^2$ for large γ and small angles θ [Dol93]. Therefore typical angles of TR emission are $\theta \approx 1/\gamma$.

For high γ the medium can be treated as an electron gas [Art75], which allows the approximation for the dielectric constant $\epsilon = 1 - \omega_p/\omega = 1 - \xi^2$. ω_p is the plasma frequency of the medium given by $\omega_p = \sqrt{\frac{4\pi n e^2}{m_e}} = 28.8 \sqrt{\rho \frac{Z}{A}} eV$. (n : number of electrons, m_e : electron mass, ρ : density of medium, Z, A : atomic number/weight of medium material)

At small angles θ and at high γ the term $(1 - \beta \sqrt{\epsilon - \sin^2 \theta})$ from Eq. 3.1 has a minimum for $\xi \approx 1$. Due to large deviations of ξ from 1 for high frequencies $\gg \omega_p$, the main part of the TR spectra falls into the energy range of X-rays.

The angular distribution can be approximated with:

$$\frac{dW}{d\omega d\theta} = \frac{2\alpha}{\pi} \theta^3 \left(\frac{1}{\gamma^{-2} + \theta^2 + \xi_v^2} - \frac{1}{\gamma^{-2} + \theta^2 + \xi_m^2} \right) \quad (3.2)$$

where $\alpha = 1/137$ is the electromagnetic coupling constant, ξ_m and ξ_v represent the values for the medium and the vacuum case.

Integration of eq. 3.2 over θ and ω in the medium-vacuum case ($\xi_g = 0$) yields the energy:

$$W_{TR} = \frac{1}{3} \alpha \omega_f \gamma. \quad (3.3)$$

This formula is very important for using a TRD to identify particles as it shows a linear dependence between the radiation yield and the γ of the particle.

The transition yield per boundary is small, for typical materials the average number of photons per boundary is $\ll 1$. Therefore one uses multiple layers of material.

For multiple layers of boundaries one has to take into account that a particle has to travel a distance of the order of magnitude of one phase length before emitting another photon. This is due to the fact that the energy transfer at relativistic energies from the particle to the medium is very small. In the medium-to-vacuum case this distance z , the so called formation length, is given by:

$$z \approx \frac{2c}{\omega(\gamma^{-2} + \theta^2)}. \quad (3.4)$$

For an optimal photon yield the thickness of each material or gas layer should (at least) be of the same order of magnitude as the formation length in the medium. Otherwise the output will be reduced by interference factors. As the emitted TR photons are partially absorbed within the following layers a saturation limit exists, where the amount of TR which leaves the material does no longer increase with the number of layers.

The effective number of layers N_{eff} represents the number of material layers if no absorption occurs, that are necessary to emit the same amount of radiation, that is emitted from N layers of material, when taking absorption into account:

$$N_{eff} = \frac{1 - e^{-N\sigma}}{1 - e^{-\sigma}}, \quad \text{with } \sigma = (\mu_f \rho_f t_f) + (\mu_g \rho_g t_g), \quad (3.5)$$

where μ represents the mass attenuation coefficient, ρ the density and t the thickness of the foil and the gas layer. In the medium to vacuum case the gas term vanishes.

An upper limit for the effective number of layers is given for $N \rightarrow \infty$ by $N_{eff} \rightarrow (1 - e^{-\sigma})^{-1}$. This establishes a limit, where an increase of the number of boundaries in a radiator increases the amount of TR leaving the radiator no more.

3.2 Design Considerations

Designing a TRD usually demands a trade-off between physics necessities and restrictions, some of which have been described in the previous section, and technical issues like the available space and mechanical stability. TRDs have been employed in various experiments, but the use of a TRD for particle identification at LHC energies poses various new challenges.

In this section the requirements on the design of the ALICE TRD are explained and the design and setup of the ALICE TRD is described.

3.2.1 Performance Issues

The main reason for introducing the TRD into ALICE is the very good electron-pion separation capability, as a very efficient electron identification is crucial to various measurements in heavy ion collisions carried out by ALICE. A comprehensive overview of the physics tasks of the ALICE TRD and the design restrictions arising from these can be found in [TRD01].

The TRD will play an important role in the measurement of various vector mesons via their leptonic decay channel, especially of the J/Ψ meson. As the ITS facilitates to distinguish between primary and secondary J/Ψ mesons, it will be possible to measure the B-meson production cross section. It will also be possible to measure semi-leptonic open charm and beauty decays of hadrons. Together with the muon arm and other central barrel detectors it will be possible to cover a rapidity interval of $-4 \leq \eta \leq 4$. Moreover, the TRD will be used as a trigger for jets as well as for the measurement of Υ mesons. In $p + p$ collisions the TRD is expected to measure the p_T spectra of D and B mesons down to less than $100 \text{ MeV}/c$, a region which could not be examined in other experiments so far. Like in heavy ion collisions the TRD is going to be used as a trigger for particles with high p_T .

These tasks have resulted in a set of requirements put forward in [TRD99] and [TRD01]: For transverse momenta of $> 3 \text{ GeV}/c$ a pion rejection of factor 100 is aimed at, which is especially important for identifying light vector mesons.

Furthermore it is important to be able to combine the TPC results with those from the TRD in order to optimize particle identification and momentum resolution. This will be ensured by a momentum resolution of 5% at 5 GeV, which is foreseen in the design.

The TRD has to be able to deal with a multiplicity of up to 8000, besides a high granularity, this also requires the capability to handle a high occupancy.

In order to minimize additional background electrons produced by photon conversion in the TRD and electron energy losses by bremsstrahlung the thickness of the TRD should be kept to a minimum.

Besides these physics requirements there are practical limitations: Due to the finite space available within the spaceframe for the TRD, the design has to be self supporting without the need for a rigid external support structure.

3.2.2 Setup of the ALICE-TRD

The whole TRD will consist of 540 individual modules, in which TR is produced and registered. These modules are grouped into stacks of 6 modules. Along the beam pipe, which defines the z -axis, there are 5 segments with one stack each (see Figure 3.1. In ϕ , which is the angle around the z -axis, there are 18 segments with one stack each.

The TRD modules consist of three major parts (see figure 3.2: the radiator, a multi-wire proportional readout chamber and the front-end electronics needed to read out the wire chamber. In the following sections these three parts are described in more detail.

The Radiator

Within the TRD, the radiator has to fulfil various tasks. Besides the main task, yielding a sufficient amount of TR from a limited thickness, there are also mechanical issues, partly caused by the necessity to keep dead material to an absolute minimum, in order not to interfere with the measurements of the detectors behind the TRD. Mainly three different types of radiators were considered for the TRD: foil stack radiators, fibre mat radiators and radiators made of foam.

foil stack radiators, can be understood comparably easy but as the spacing of the foils has to be very accurate they are difficult to realize. Fibre mats can be described similarly to foil stacks and they are easier to handle as the boundaries already exist within the mats. Foams were considered especially due to their very good mechanical properties.

Tests have shown that although foils would give the best TR yield, fibre mats showed only slightly worse yields, but were much lighter. As foams could only compete for large thicknesses, which exceeded the initial specifications for the radiator, it was decided to use fibre mat radiators. [TRD01]

The final design foresees a sandwich construction: There are two cover plates made of *Rohacell HF71* foam. This foam has been chosen as it combines good mechanical rigidity and low density with a good contribution to the TR production. In order to increase the mechanical rigidity the cover plates are reinforced with carbon fibre mats. In order to ensure gas tightness and protection against humidity, aluminium coated mylar foil is glued to this carbon reinforcements.

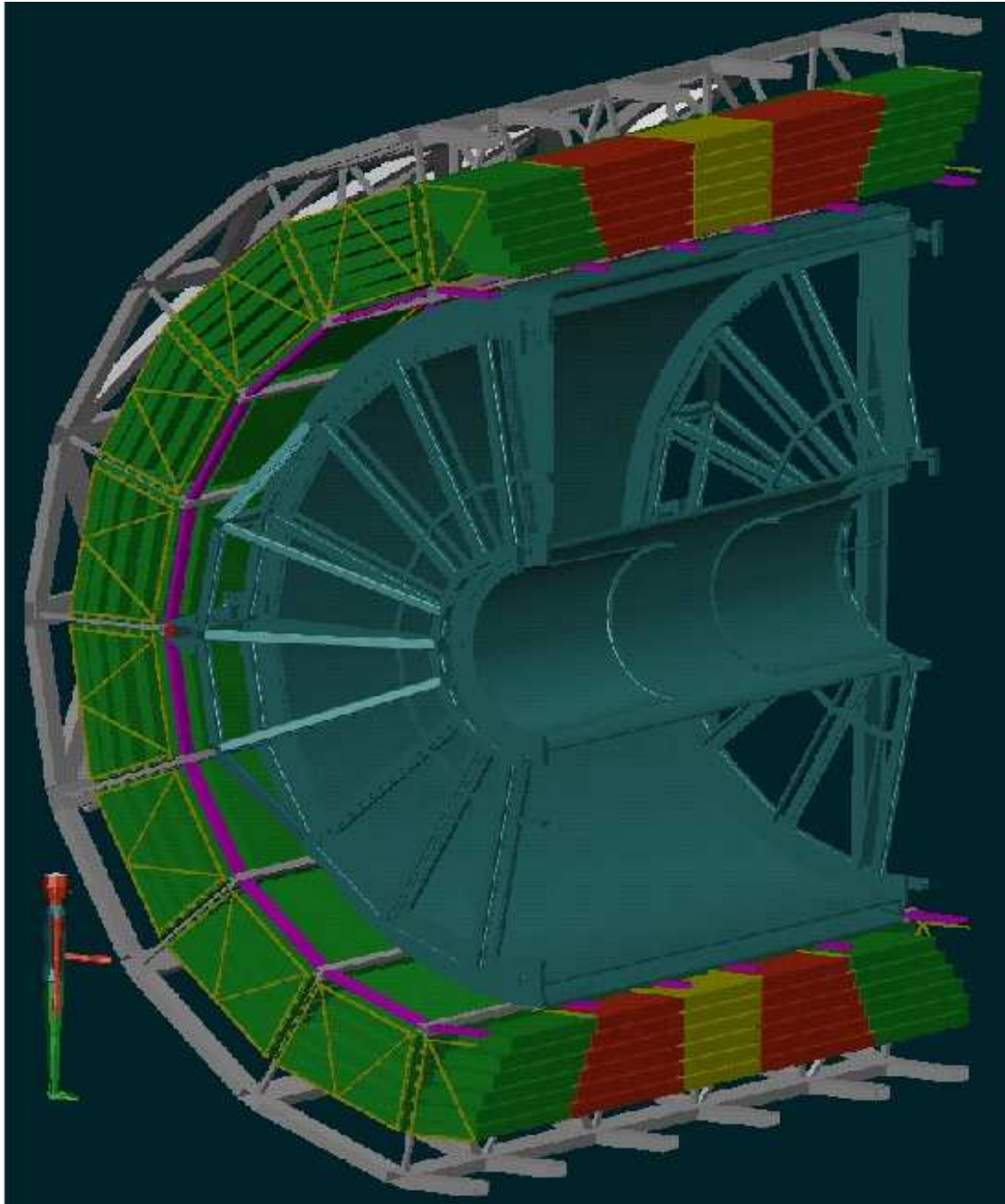


Figure 3.1: Cut through the central barrel of ALICE, showing the alignment of the 540 TRD-modules around the beam line [TRD05]

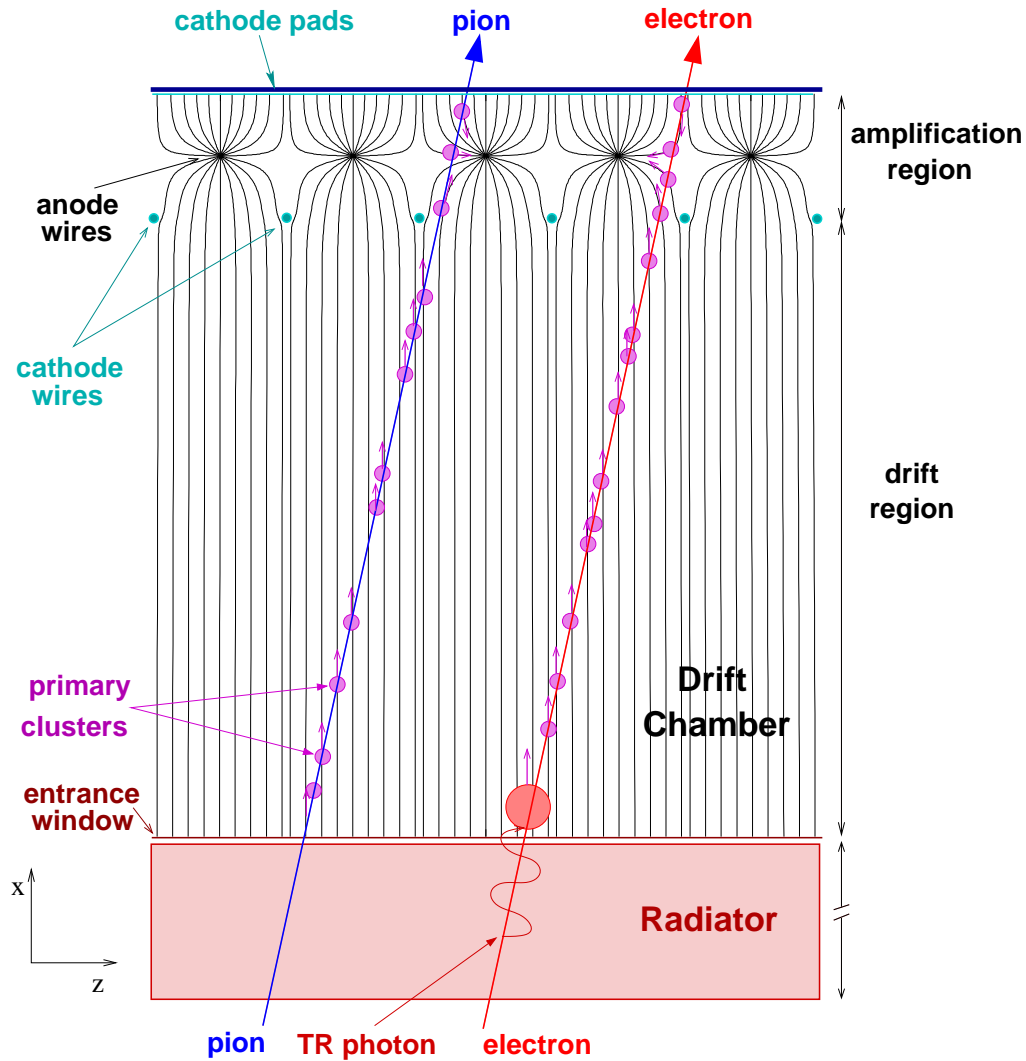


Figure 3.2: Basic setup and function of the TRD [TRD05]

The window of the readout chamber, that serves as drift electrode, is glued directly to the radiator. Deformations of the cover plate by gravity or the gas pressure would cause a distortion of the electric field within the readout chamber and thereby performance losses, due to different drift times of the electrons. In order to optimize the mechanical rigidity of the radiator, the two carbon enforced covers are spaced by a grid structure of crossbars which are also made of *Rohacell HF71*. Within the chambers of this grid structure, stacks of fibre mats are placed (see Figure 3.3).

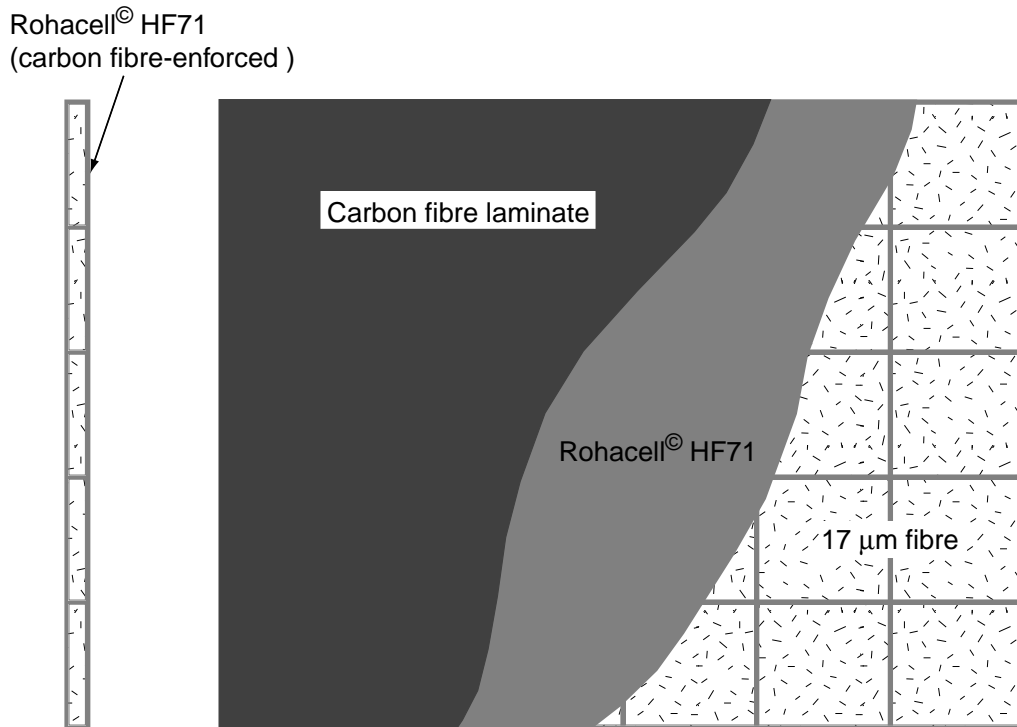


Figure 3.3: Sketch of the sandwich composition of the TRD [TRD01]

The Readout Chamber

Each TRD module is equipped with a multiwire proportional readout chamber. Within these chamber a traversing particle, especially an electron or a pion, will create a trace of electrons and ions which can be read out. The possibly produced TR will create additional electrons, which will allow a separation of various particles via the shape of the pulse (s. fig. 3.4)

The readout chamber is positioned on the radiator cover. An aluminium coated mylar window is glued directly to this cover. A voltage of -2.1keV will be applied to it and serves as drift voltage. The drift region ends at the cathode wire plane. To ensure a homogenous field within the drift region a number of copper potential strips runs along the side walls of the chamber.

It is filled with a gas mixture consisting of 85% Xe and 15%CO₂, the Xenon gas has been chosen due to its high X-ray photoabsorption cross section, which is necessary for a good detection of the TR photons. The CO₂ serves as quencher.

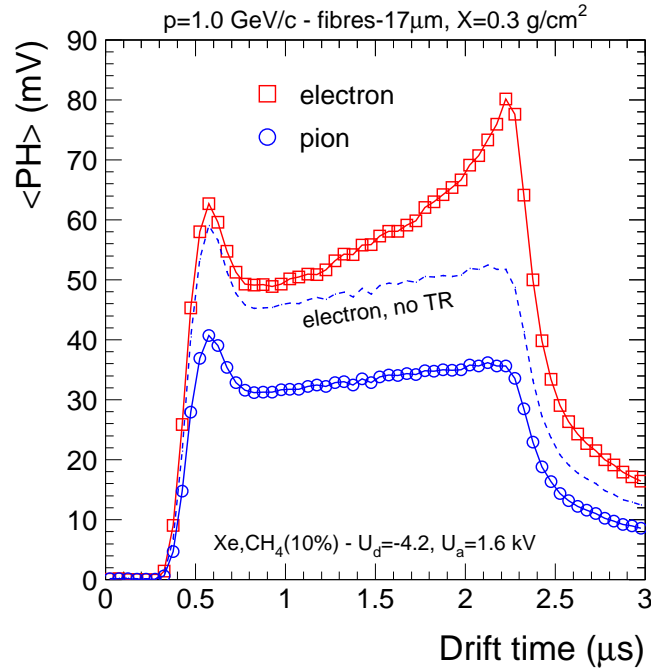


Figure 3.4: Averaged shape of the spectrum for electrons and pions, dashed line: electrons without TR [TRD01]

As the number of electrons produced directly by the initial particle together with the TR is not sufficient to produce a measurable signal, another wire plane, the anode wire plane, is positioned 3.5 mm above the cathode wireplane with a voltage of +1.4 keV with respect to the latter in order to multiply the charges by a factor of 10^4 through avalanches. The region between these two wire planes is designated as amplification region. The anode wires are positioned between two cathode wires in order to optimize charge sharing between pads. While the anode wires are spaced at 5 mm intervals, the cathode wires have 2.5 mm spacings, which is necessary to decouple the amplification from the drift region and minimize the number of ions reentering the drift region from the amplification region. The moving electrons induce a current in the pads on the pad plane, located another 3.5 mm above the anode wires. The pad plane consists of pads with widths between 5.85 – 10.35 mm and lengths of 75 – 90 mm, tilted with respect to z by an angle of 2° [Ems04]. By inverting the tilt direction of every layer the z -position resolution can be improved

significantly. In general, the pads are designed so, that the charge distributes over 2-3 pads. This makes it possible to compute a *center of gravity*, which increases the position resolution of the particle.

The back of the pad plane will be enforced for stability reasons with a honeycomb structure. 6-8 readout boards (ROB's), the number depending on the chamber size, will be mounted on the back of this layer and read the signal induced on the pads via flexible cables led through the backlayer.

Front-End Electronics

Most of the Front-End electronics is mounted directly on the ROBs on the back of the TRD. An overview is displayed in figure 3.5. Essentially, there will be a charge sensitive preamplifier and shaper (PASA) that shapes the signal from the pad before it is digitized within an ADC. The digitized signal is fed into a Tracklet Preprocessor (TPP), which does a first analysis for a possible trigger decision of the TRD. These three components will be put on one multichip module (MCM) with 18 channels, where ADC and TPP will be realized as one single chip (TRAP chip). The data acquired by each channel is merged over a tree structure of merger chips before it is sent to the GTU (global tracking unit). A detailed description can be found in [Lin04, TRD01].

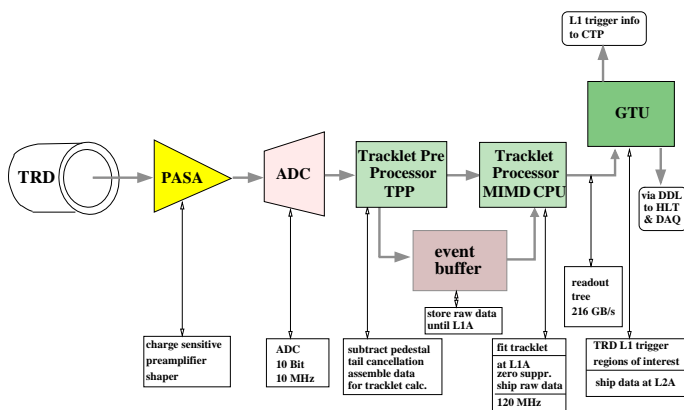


Figure 3.5: Overview over working principle of the FEE [TRD01]

4. Theoretical Background on X-rays

4.1 Generation of X-rays

X-rays are electromagnetic radiation with typical energies in the order of keV. One often distinguishes between two different basic types of X-ray radiation, depending on their production mechanism: characteristic radiation and bremsstrahlung [Kno99].

Characteristic radiation is typically produced in the electron envelope of atoms by excited electrons which drop to an available lower energy level. The emitted photon typically has an energy in the X-ray range. As the energy of the photon corresponds to the energy difference between the excited and the final state of the emitting electron, the various typical energies of characteristic X-ray radiation of a given element are labelled according to the participating shells as K-series, L-Series etc.

Excitation of the electron envelope can be produced by an electron capture process, a radioactive decay which is concurrent with the β^+ process, in which an electron, mostly one in the K-shell, is integrated into the nucleus. The atomic charge Z of the atom is reduced by one but the electrons are left in an excited state, which is de-excited by emitting X-ray photons.

A radioactive decay that is accompanied by gamma radiation can cause internal conversion. In this process an electron is ejected from the atom by interacting with a gamma photon ejected by the nucleus. This also leaves the electron envelope in an excited state that leads to de-excitation processes that typically emit X-ray radiation.

In technical application external radiation sources are often used to cause the desired excitation. One uses an external radiation source, such as another X-ray source or a radioactive isotope, which emits gamma radiation to excite the electron envelope of the target material. In order to produce the characteristic radiation in the target material, the radiation used for excitation has to have an energy larger than or equal to the desired radiation of the target material. The excitation can also be caused by particles, for example alpha particles emitted by a radioactive isotope, or by electrons.

Common X-ray tubes use an electron beam that is typically accelerated to energies in the order of keV, to cause excitation in the electron envelope of a target material. A X-ray spectrum generated by such a setup does not only contain the characteristic radiation of the target material. The electron is deflected within the target, due to this acceleration it loses its energy partly by radiation. There is an additional radiation continuum in the X-ray spectrum caused by these radiation losses, called bremsstrahlung. As these radiation losses are proportional to m^{-2} , they are negligible for heavier particles. The spectrum of bremsstrahlung spans from 0 keV to the maximum energy of the electrons. A pure spectrum of the bremsstrahlung can be obtained by choosing the absorber in such a way, that the electrons can not produce characteristic radiation. Due to its continuous nature bremsstrahlung can be a useful tool by itself.

4.2 Attenuation of X-rays in Matter

According to the Beer-Lambert law equal ways of radiation through a given material lead to the same relative attenuation of this radiation [Ger93]:

$$\frac{dI}{I} = -\mu_l(E)dx \Leftrightarrow I = I_0 e^{-\mu_l(E)x}. \quad (4.1)$$

$\mu_l(E)$ is the linear attenuation coefficient, which depends on the energy of the incident radiation. In order to be independent of the amount and state of the attenuating material, the mass attenuation coefficient¹ μ_m is introduced: $\mu_m = \mu_l/\rho R$, which can be related to the total atomic attenuation cross section σ_{tot} for materials consisting of a single element.[Ger86]

$$\mu_m = \frac{N_A}{A} \sigma_{tot} \quad (4.2)$$

(N_A : Avogadro constant, A : atomic weight). For photon energies of several keV, σ_{tot} is given by the sum of the cross sections for the photoelectric effect, coherent scattering and incoherent Compton scattering: $\sigma_{tot} = \sigma_P + \sigma_R + \sigma_C$.

Typically, the photoelectric absorption is dominating for lower energies. Starting at energies in the order of magnitude of 10 keV, Compton scattering contributes the most significant share to the total photon attenuation cross section. The contribution

¹Often the term *mass absorption coefficient* is used for this quantity. As this term has been used ambiguously in literature, the International Commission on Radiation Units and Measurements (ICRU) has proposed the term *mass attenuation coefficient* [Hub99].

of coherent scattering at X-ray energies is small. Other effects, as pair and triplet production or the nuclear photoeffect, are only possible at energies in the MeV scale and can therefore safely be neglected at X-ray energies.

$\mu(E)$ has been empirically examined over a wide range of energies and for a great number of materials and elements.

Additionally, there have been various attempts to give an empirical or semi-empirical parametrization of these data which will be discussed in chapter 7.1.

Chemical compounds of different elements can be easily described with a weighted sum over the mass absorption coefficient for the different elements

$$\mu_{\text{sum}} = \sum_i x_i \frac{A_i}{N_A} \mu_i, \quad (4.3)$$

where A_i is the atomic weight of the element, μ_i its mass absorption coefficient and x_i the number of atoms of the element per molecule [Zsc89].

4.3 Measuring X-rays

X-rays can be detected via their interaction with matter. The possible types of interaction have been sketched out shortly in the previous section.

Several detector types are suited for the measurement of X-rays. As the measurements in this thesis have been performed with a Si(Li) detector, a short overview over the principles and advantages of this detector type is given here. A typical setup is shown in Figure 4.1

A semiconductor detector is essentially a diode with a reverse bias voltage applied. Due to the steep gradient of the electron concentration at the p-n junction of a diode, charge carriers are exchanged between the two oppositely doped regions by diffusion, building up a so-called depletion region. Its size is limited by the electric field created by this process. Any free charge carrier within the depletion region will be pushed out of it due to the electric field. At the opposite sides of the junction, these electrons can be measured as electric current. As the electric field created by the charge carriers in the depletion region is not large enough to suppress recombination of the electron-hole pairs significantly and as the drift speed within the region is very slow, a bias voltage, typically in the order of magnitude of 1000V, is applied to the p-n junction. Even if the depletion region is small compared to the whole semiconducting material, the greatest part of the voltage will appear there due to its much higher resistivity,

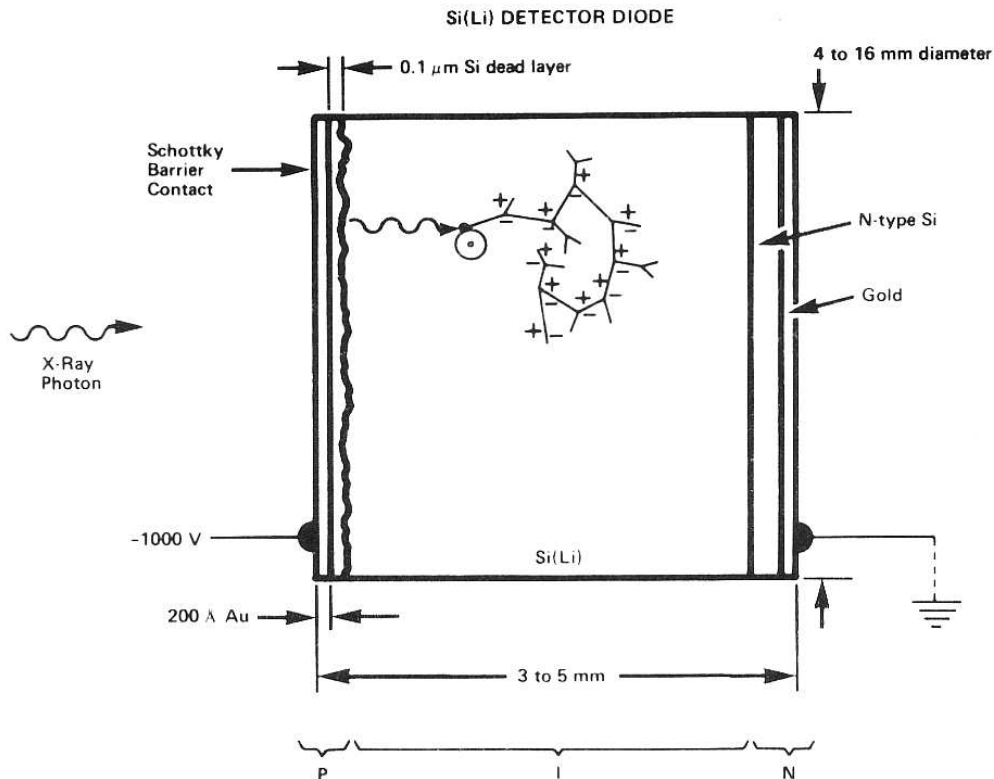


Figure 4.1: Typical Si(Li) diode detector [Ged72]

caused by the immobility of the electrons of the dopant materials. This also enlarges the size of the depletion region, which grows proportional with \sqrt{U} . As the electric field grows with U the maximum thickness of the depletion region is limited by possible breakdowns occurring at high voltages. In order to increase the thickness of the depletion region one has to increase the specific resistivity of the detector material. High purity crystals of the semiconductor material would be a very good choice, but due to the technical difficulties concerning the creation of such crystals in reasonable sizes, other techniques have been developed. A common solution is to use compensated materials. Lithium compensated Silicon (Si(Li)) is often chosen for X-ray detectors. It is possible to drift Lithium ions into a p-doped Silicon crystal so that the p-doping is compensated for and no space charge exists in the compensated region. As Lithium is typically diffused onto a surface of silicon and then drifted into it, the process leaves the side, where the Lithium was initially diffused to, as n-doped and the opposing, where no or only a few Lithium ions could be drifted

to, as p-doped. The compensated region between these two is often designated as *i*-region, referring to the fact that the achieved resistivity, for Si(Li) diodes typically in the order of magnitude of $10^5\Omega$, is near that of intrinsic crystals.

The increase in size of the depletion region is important, as this is the active volume of the detector. Electron-hole pairs created in this region are separated by the strong electrical field and cannot recombine. They can be measured as a current between the p- and the n-doped side of the semiconductor. As the number of electron-hole pairs created by X-rays is proportional to the energy of the incident radiation, the voltage of the output pulse will be, too. Due to the small band gap ϵ of semiconductors the number n of electrons created by the radiation, which is given by

$$n = \frac{E}{\epsilon} \tag{4.4}$$

for a certain energy E [Ged72], is high, compared to other detector types, thus leading to very good energy resolution.

5. Experimental Setup

5.1 Motivation and Tasks

As discussed in chapter 3, a good TR yield is crucial for the ALICE TRD. This yield is obviously not only influenced by the production efficiency but also by the absorption properties of the radiator.

In order to understand the absorption on a quantitative basis and - foremost - to ensure homogenous properties of all radiators produced, a test stand has been developed, with which the X-ray absorption of the full radiators as well as of the components can be measured.

Measurements of the TR spectrum have shown that the energy of the TR photons produced by ultrarelativistic electrons is peaked at ≈ 10 keV. [Bus04, TRD01] In order to be able to take measurements over the energy range of interest quickly, it was decided to carry out the measurements with a X-ray generator producing bremsstrahlung and to use a Si(Li) detector with good energy resolution for the detection of the X-ray spectrum, so that the energies up to 10 keV can be covered in one single measurement.

Basically, the spectrum produced by an X-ray generator is measured with a Si(Li) detector with and without an absorber between generator and detector. The absorption can be determined by calculating the quotient of the two spectra.

5.2 Overview

The setup is situated in the rooms of the *Institut für Kernphysik (IKP)* in Münster. (see Figure 5.1)

The detector and the X-ray generator together with the necessary HV-supply are located on a mounting which has a guide for the absorber materials. The necessary electronics are situated in a 19" rack nearby, together with the PCs which actually record the data. The recorded spectra are then processed with the help of the data analysis package *ROOT* [ROO04] macros.



Figure 5.1: View of the setup situated at the IKP, Muenster

5.3 Test Stand

The absorber mounting was designed to hold entire radiators as well as individual parts of the radiator. Its main structure consists of KANYA-profiles. The guide for the absorber materials can be adjusted in height in steps of 11.5 cm, so that every cell of the grid within a radiator can be targeted. It is equipped with rollers, so that the absorber material can be moved through the X-ray beam horizontally. The detector and the X-ray generator are positioned at opposite sides of the guide (see Figure 5.2), the generator is mounted on a pedestal so that the height of the beam output matches the height of the entrance windows of the detector. The detector sits on a sled that can be moved in beam direction. This sled is directly screwed to the absorber mount. The distance between the output of the X-ray generator and the detector window is 17 cm.

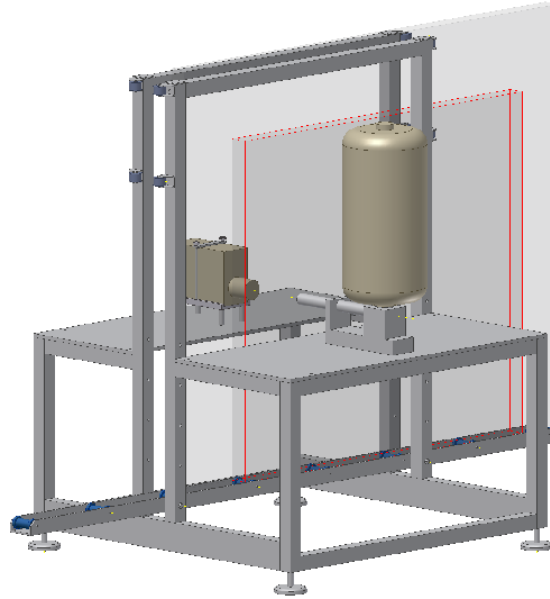


Figure 5.2: CAD sketch of the absorber mount [Ver04]

5.3.1 The X-ray Generator

The X-ray generator was provided by the JINR, Dubna¹ (see Figure 5.3).

It delivers a bremsstrahlung spectrum up to 10 keV. The X-ray tube of the generator is equipped with an Ag-cathode. The characteristic K-shell photons of Ag have an energy of more than 20 keV, the L-shell photons have energies below 3 keV [Tho01], therefore a clean bremsstrahlung spectrum can be obtained for energies from 3-10 keV. The necessary high voltage of -10 keV is delivered by an *Applied Kilovolts HP10N* high voltage supply that has been upgraded with a precision current monitor. As the X-ray generator has no option to monitor the tube current directly, the current is monitored via the high voltage supply instead.

As the Si(Li) detector is not suited for high count rates of $\gg 1000\text{cts}/\text{sec}$, the tube current has been adjusted to $\approx 2\mu\text{A}$. The radiation from the tube is collimated by a lead collimator with a circular opening with a diameter of 5 mm. In order to decrease the count rate at the detector further, a copper tube with 3 mm inner diameter has been put into the lead collimator.

¹Joint Institute for Nuclear Research

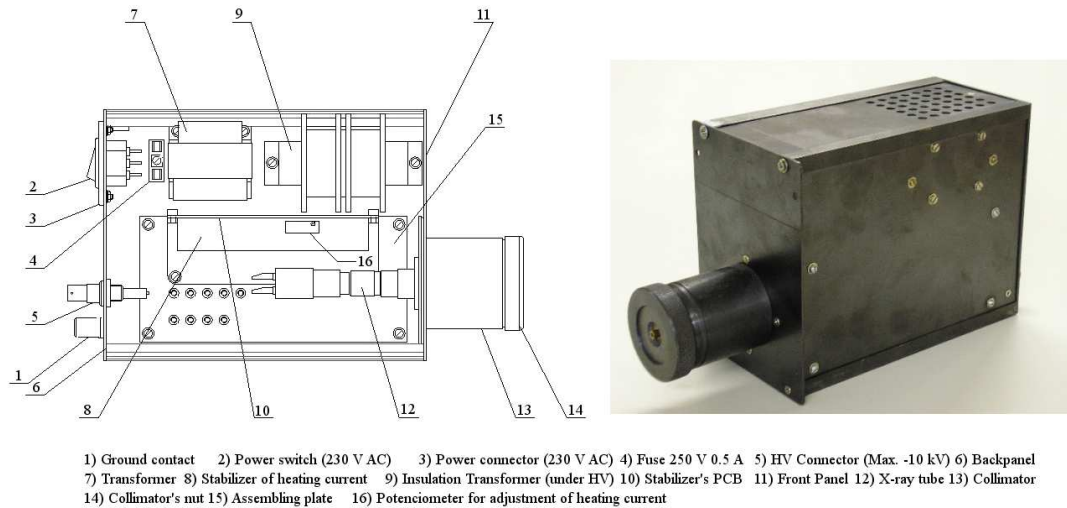


Figure 5.3: Sketch of the X-ray source [Yur03]

The spectrum obtained from the tube is peaked at $\approx 8.5\text{keV}$ (see Figure 5.10).

5.3.2 The Si(Li) Detector

The X-ray measurements for this thesis are carried out with a *KeveX 3201-AA-80* Si(Li) detector. It has an active area of 80mm^2 and a Beryllium entrance-window with $12.5\ \mu\text{m}$ thickness. The energy resolution has been specified originally to be better than $175\ \text{eV}$ at $5.9\ \text{keV}$ and 1000 counts per second, but this value has degraded to $\approx 430\ \text{eV}$ at $8.04\ \text{keV}$ (see chapter 5.5.2 for details).

The detector is cooled with liquid nitrogen at any time in order to reduce background by thermal excitation in the semiconductor.

A *KeveX 2002A* preamplifier with pulsed optical feedback has been mounted directly to the detector. The necessary bias voltage of -1000V for the detector is supplied by a *KeveX 4600* NIM-module. A *Canberra 1713* spectroscopy amplifier is used to amplify and shape the signal. It also provides the power for the preamplifier. It is set to a coarse gain of 300 , a fine gain of 3.30 , and a shaping time of $1\ \mu\text{s}$. The baseline restorer is set to *high*, as the count rates used are high for a Si(Li) detector. The detector has been equipped with a collimator with a 2mm opening in order to obtain the desired count rates of \approx in measurements with the X-ray generator.

5.4 Data Acquisition and Control

Most of the data has been taken with a Labview-based Data Acquisition (DAQ) and control system, which has been developed for this experiment. The first measurements have been taken with an Aptec MCard DAQ system that had originally been used with the detector. An overview over the DAQ system is shown in Figure 5.4.

5.4.1 Aptec MCard System

The MCard system is an out-of-the-box DAQ system, consisting of an ADC-NIM module (*Tracor Northern TN-1212A*) which is connected to a PC-ISA card that hosts a Multi Channel Analyzer (MCA). The PC software runs on Windows 3.11 for Workgroups and MS-DOS 6.20. The operation of the MCA as well as the DAQ can be controlled via a software interface (*Aptec PCMCA/WIN Version 5.30*). The MCA and ADC used are both set to the maximum 12bit resolution. The system automatically compensates for its dead time and can acquire data for specified live-times. The spectra taken are saved as text datafiles for further analysis.

During the first measurements, the ADC was connected directly to the output of the *Canberra 1713* amplifier, when the Labview based DAQ system was operational, this amplifier signal was routed through an analog fan out built by the electronics workshop of the IKP to allow simultaneous measurements with both DAQ systems. The current and the voltage of the HV-supply are monitored manually via LCD panelmeters (*Conrad SI-70004*) connected to the monitor outputs of the HV-supply.

5.4.2 Labview System

The Labview-based DAQ and control system has been developed specifically for this setup. It is possible to acquire and save spectra, to monitor the current and the voltage of the HV supply and to control it.

The system is based upon a program written with *Labview* that makes it possible to control the setup and acquire data. The program runs on a standard PC equipped with a *National Instruments 6040 E* DAQ card for data in- and output. External NIM electronics are used to shape the signal adequately for the DAQ card and to generate a trigger pulse.

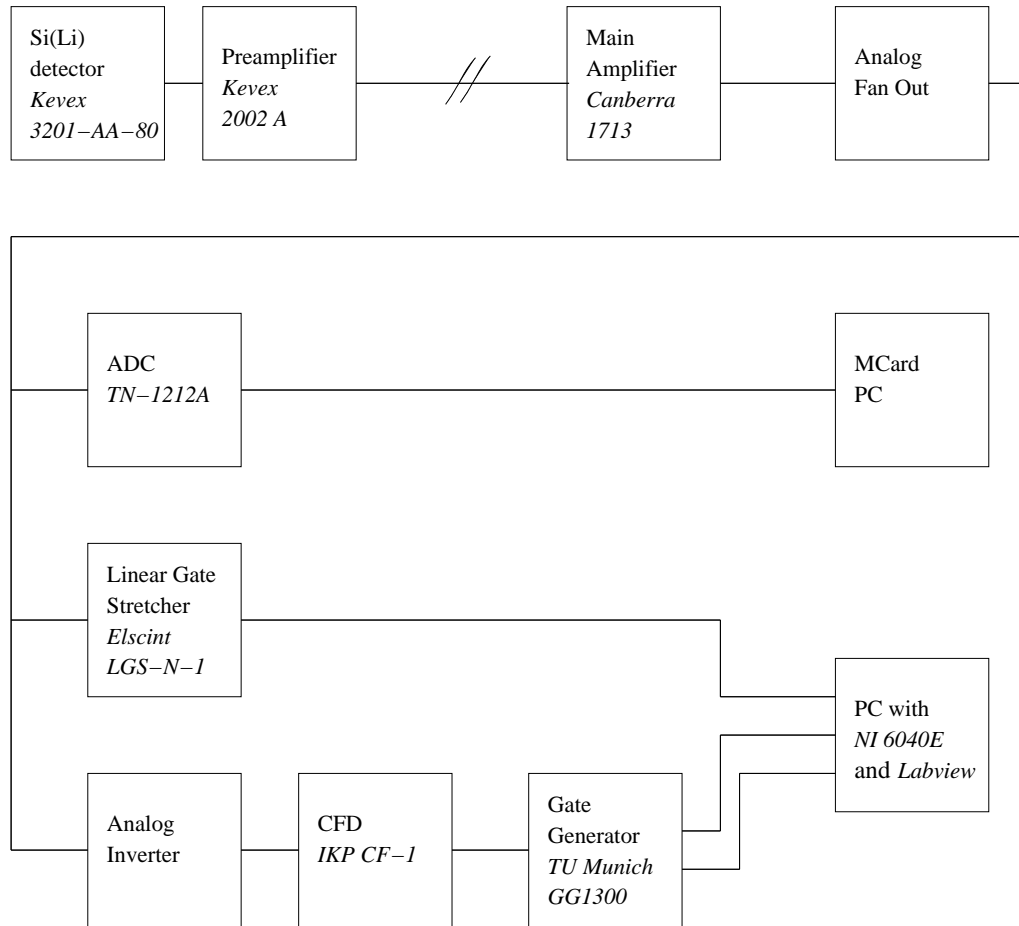


Figure 5.4: Schematic of the DAQ system

External Electronics

The original pulse of the *Canberra 1713* amplifier is routed to multiple connectors by an analog fan out, as described in the last section. Two branches necessary for the Labview-based DAQ system are connected to the outputs of the analog fan out, a third is connected to the MCard system.

One branch generates a TTL pulse from the analog signal. This is done with a constant fraction discriminator (Model *CF1*, electronics workshop of the IKP). As the input of this device needs pulses with negative polarity a signal amplifier is used to invert the positive pulse from the main amplifier with an amplification factor of 1. The threshold of the discriminator is set to -135 mV in order to exclude noise. The TTL pulse generated is widened to $1.44 \mu\text{s}$ by a gate generator (model GG

1300, built at the TU Munich) with two outputs that are both connected to the DAQ card, one signal is used as trigger signal, the other signal is used for the digital counter.

The other signal branch from the analog fan out supplies the analog pulse to the DAQ system. As the relative position between the gate signal and the analog pulse shifts with the height of the pulse, a Linear Gate Stretcher (*Elscint LGS-N-1*) is used to create an analog signal that is not sharply peaked but has a plateau with the value of the peak of the original signal. The width of the plateau is adjusted to $4.4 \mu\text{s}$.

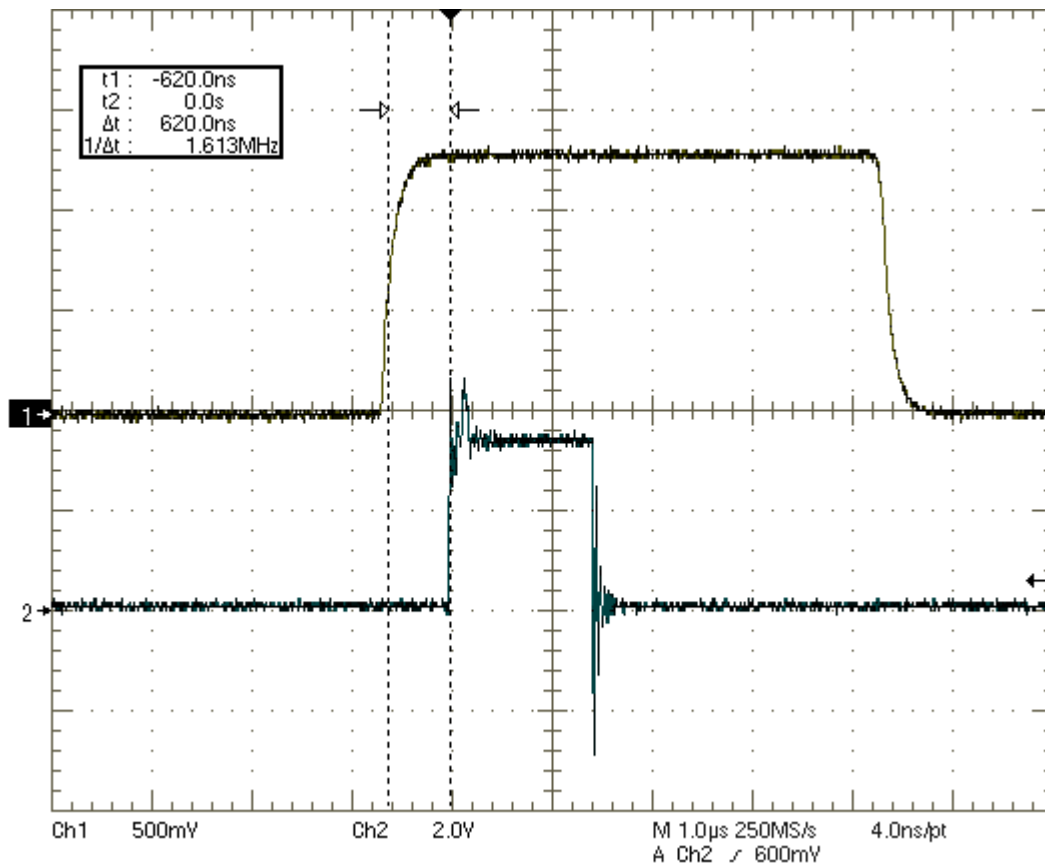


Figure 5.5: TTL pulse and analog signal from the detector

The delay times of the Linear Gate Stretcher and the gate generator are adjusted so that the gate arrives during the plateau generated by the LGS. The TTL pulse has a delay of 600 ns with respect to the analog signal (see Figure 5.5).

DAQ Hardware

The data for the Labview based system is acquired through a *National Instruments NI 6040E* multipurpose I/O card. It offers 16 analog inputs and 2 analog outputs each with 12 bit ADCs and 8 digital I/O ports as well as 2 counters and connectors for digital trigger and gate signals. A shielded connector box (*National Instruments SCB-68*) is used to connect the signals from the electronics.

Three analog inputs are used, all set to an input range of 0 – 10V. The first analog input is connected to the analog signal from the LGS, the second and third analog input are used to monitor the high voltage supply. One input is connected to the voltage monitor, the input values are proportional to the output voltage 0 – 10 kV, the other is connected to the current monitor. Here the input range of 0 – 10 V translates to 0 – 1 mA.

The analog output is used to control the high voltage via the external control connector of the HV supply. Once ramped up, the control voltage can be supplied by a very stable external power source (*Heinzinger LNG 16-12*), to allow, for example, for reboots of the PC without having to turn of the X-ray source. A capacitor buffered switch permits to choose between the two voltage supplies.

One of the two output signals of the gate generator is connected to the trigger connector for the first analog input that receives the analog pulse from the LGS, the other gate signal is connected to a digital counter.

Labview Program

The necessary software has been written with *Labview 6.1i*² running under Windows XP Professional on an AMD Athlon 600 MHz with 256 MB RAM.

It consists of several modules that facilitate the control of the high voltage, to take longtime measurements of the HV current and voltage together with the count rate at the detector, and to acquire and save an X-ray spectrum together with the duration of the measurement and the current and voltage of the HV supply.

The modules for the control of the voltage can ramp the voltage to a specified value over a specified time. The voltage and current of the HV supply, as well as a time stamp, are saved to a data file at regular intervals.

²Labview is a graphical programming language by National Instruments with powerful DAQ drivers. Predefined subroutines for data I/O are available for various PC-cards.

The module for monitoring the time dependence of the current and the count rate saves a time stamp together with the values of the current, the voltage monitor and the current count rate averaged over a user-defined time interval to a data file.

X-ray spectra are acquired with the third module of the program. Once the measurement is started the voltage from the first analog input, which is connected to the analog pulse from the detector, is read to a buffer, whenever a trigger signal is given. The values in the buffer are written to a data file at user-specified intervals. Once the initially preset time is reached or surpassed, the measurement is stopped and the buffer is emptied. The digital counter runs simultaneously with the measurements, giving the total number of counts for quick reference. The saved data is then post-processed by a function working similar to an MCA, which computes a pulse height diagram with 4096 channels corresponding to the 12 bit resolution of the ADC of the analog input. This pulse height diagram is then saved to a data file. The final processing of the data acquired, including corrections for dead time and renormalization to identical live times, is done via ROOT programs (see chapter 5.6).

5.5 Calibration of the Setup

5.5.1 Energy Calibration

The energy calibration of the setup was done with a variable X-ray source, consisting of an ^{241}Am -primary source that emits gamma-radiation of $\approx 60\text{keV}$. A number of targets can be put in front of this source. The gamma radiation excites the electron envelope of the target material, so that, depending on the target, photons with discrete X-ray energies are emitted. The available targets are: Copper, Rubidium, Molybdenum, Silver, Barium and Terbium.

Spectra are measured for all six of the targets. The K_α and K_β peaks are used for the energy calibration, as they are the strongest. The position of these peaks is determined by a gaussian fit with a ROOT macro. As the energy resolution of the detector does not permit to resolve the fine structure of the $K_{\alpha,\beta}$ averaged values for these lines, given in the documentation of the source, are used.

Plotting the peak position against the corresponding energy permits to deduce a linear dependence between the channels of the MCA and the energy of the incident X-ray photons via a fit to the data.

Four calibrations were done, the first three with both, the Labview and the MCard system, the last one only with the Labview system. They were done between January and October 2004. The additional calibrations were necessary due to small adjustments or repairs of the setup. In Table 5.1 the coefficients for the calibration fits can be seen. An example is shown in Figure 5.6. The standard deviation σ of the gaussian fits has been used as the error of the data points. The differences between the coefficients for the MCard and the Labview system are due to the different ADCs of the two systems.

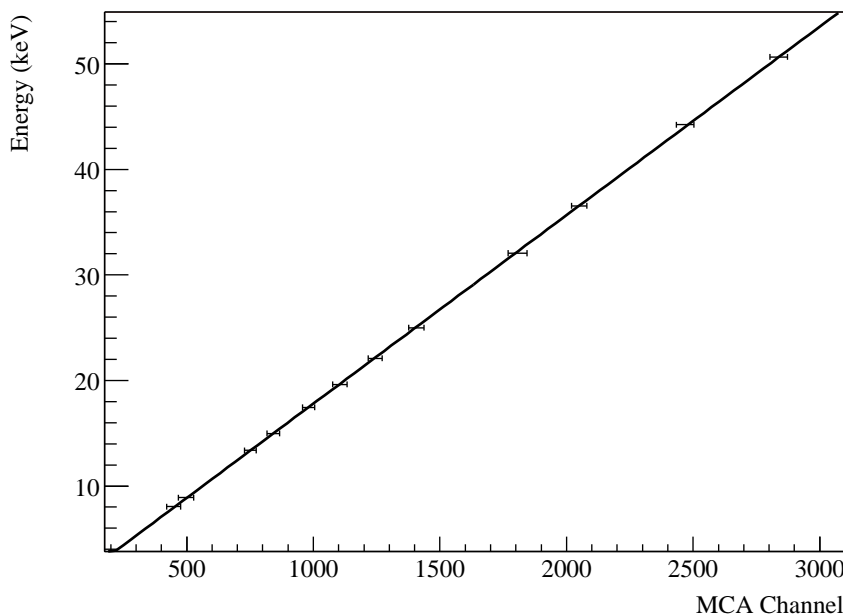


Figure 5.6: Plot for Calibration 1, Labview

5.5.2 Energy Resolution

The energy resolution capabilities of the setup can be characterized via the Full Width at Half Maximum (FWHM) of the peaks in the spectra used for the calibration.

The FWHM dE of a peak can be obtained from the standard deviation σ of the fit via $dE = 2\sqrt{2\ln 2}\sigma$.

| Calibration Index | Labview | | MCARD | |
|-------------------|-----------|------------|-----------|------------|
| | p[0] | p[1] | p[0] | p[1] |
| 1 | 0.0178525 | -0.0518315 | 0.0142984 | -0.208927 |
| 2 | 0.0178874 | -0.0178603 | 0.0143996 | -0.265004 |
| 3 | 0.018136 | 0.00344985 | 0.0146108 | -0.0812147 |
| 4 | 0.0179418 | 0.114836 | n/a | |

Table 5.1: Coefficients for the linear equation $E = p[0] * x + p[1]$ where E is the energy in keV and x the channel number

The Cu-K $_{\alpha}$ line at 8.04 keV has a FWHM of 430 eV. Typically Si(Li) detectors achieve resolutions less than 200eV at these energies. The properties of the detector used in this experiment, which was available at the IKP, have degraded, especially due to a loss of vacuum several years ago and a period of time following this, during which it was not cooled with liquid nitrogen. In this time impurities settled on the Si(Li) crystal, causing a degradation of the electric properties.

5.5.3 Determination of the Dead Time

The dead time was determined via a two-source method, as a more exact technique using a pulse generator could not be applied due to the lack of a pulser input on the components of the setup.

Two variable X-ray sources of the type used for the energy calibration were used for the dead time measurements. Each one was positioned ≈ 5 cm away from the entry window of the detector at an angle of $\approx 45^{\circ}$ to the beam direction.

Three measurements were carried out: Both sources together and each source separately. In all measurements the Terbium target was used as it offers the highest photon yield. For each measurement the spectrum was recorded for 60 minutes with both, the MCard and the Labview system. The count rates for these measurements are shown in Table 5.2.

The dead time can be calculated from the individual measurements using the formula [Leo87]:

$$\tau = \frac{R_1 R_2 - \sqrt{R_1 R_2 (R_{12} - R_1)(R_{12} - R_2)}}{R_1 R_2 R_{12}}. \quad (5.1)$$

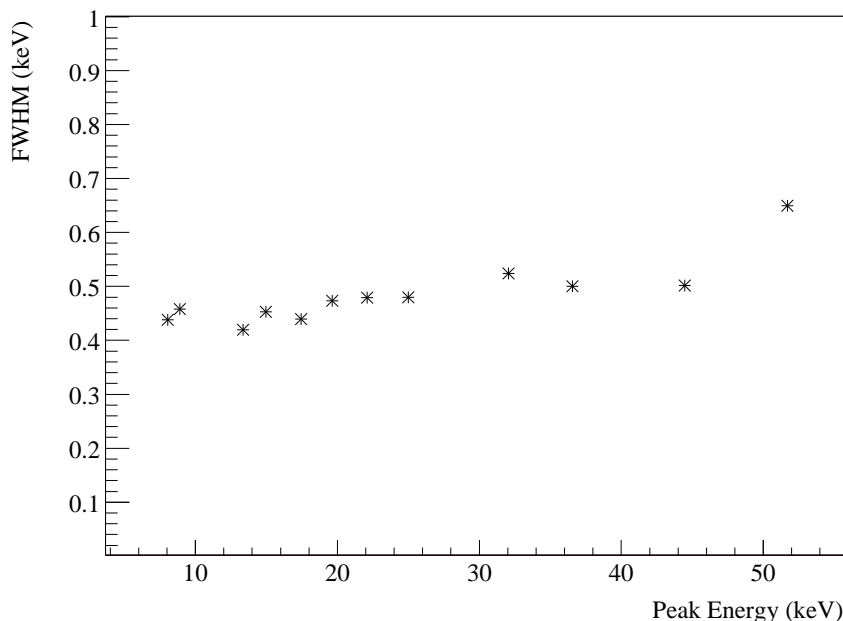


Figure 5.7: Energy resolution: dE vs E (each in keV) for values of calibration 4 (Labview)

R_1 and R_2 represent the observed count rates of the individual sources and R_{12} represents the count rate of the combined sources.

| | Count rate [1/s] | |
|------------------------------|------------------|--------------|
| | Labview system | MCard system |
| Single source 1 (R_1) | 402.56 | 384.06 |
| Single source 2 (R_2) | 519.58 | 494.19 |
| Sources 1 and 2 (R_{12}) | 917.33 | 866.93 |

Table 5.2: Count rates for the two systems

The deadtime of the Labview system was determined to be $\tau_{LV} = 11.565 \pm 0.485 \mu\text{s}$, for the MCard system it is $\tau_{MC} = 30.201 \pm 0.513 \mu\text{s}$. The errors were obtained by varying the count rates, the systematic error is typically larger and can be 10 – 15% [Leo87]. This results, for example from displacements of the sources between measurements or a not fully symmetric setup. For the calibration data the built-in

live time correction of the MCard system differs from offline correction with this dead time by less than 0.5%. Although this deviation is not within the mentioned errors above, it can be explained assuming a systematic error of 15%. Therefore the online correction is used for the measurements done with the MCard system.

5.6 Offline Analysis

The datafiles containing the spectra are transferred to another PC running under *Suse Linux*, the analysis is done with *ROOT 3.03*.

All spectra are read from the data files into histograms. The data taken with the Labview system has to be corrected for dead time. This is done by multiplying the dead time τ with the number of events in each spectrum and then subtracting the result from the time of the measurement in order to obtain the live time. In order to be able to compare different spectra, all are then renormalized to the preset live-time. This is not necessary for data acquired with the MCard system, which features online dead-time correction.

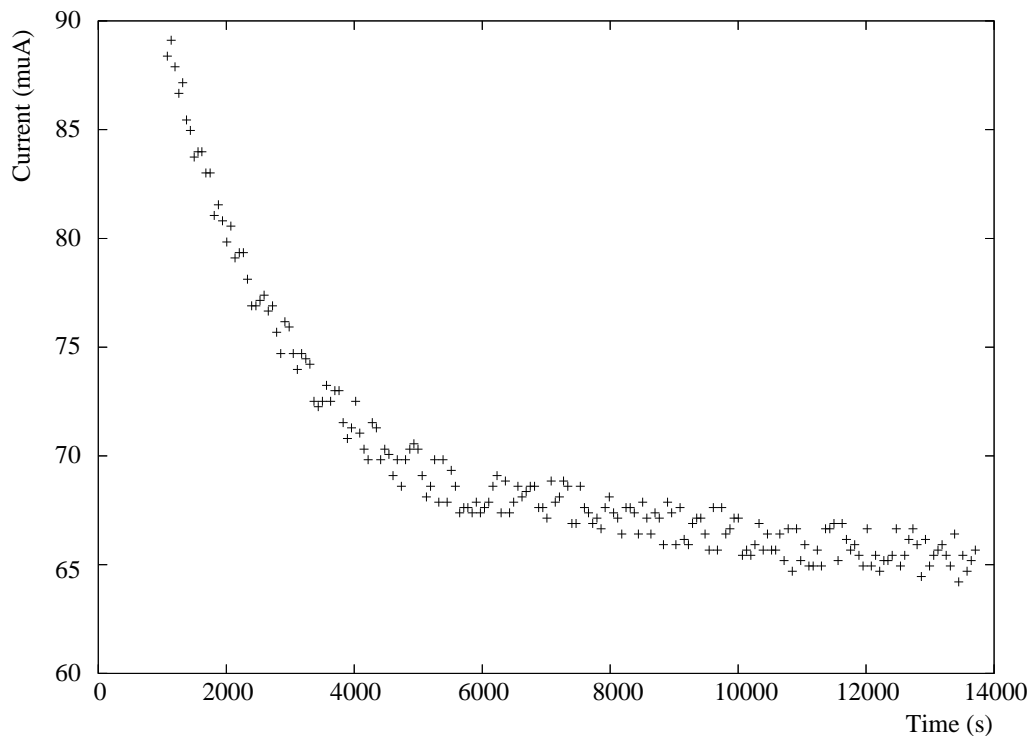


Figure 5.8: X-ray tube current as function of time

All spectra are then corrected for changes in the current of the X-ray generator. Due to warming, the current decreases as function of time (see Figure 5.8). After > 2 hours, the decay can be assumed to be linear. As can be seen in Figure 5.9, the count

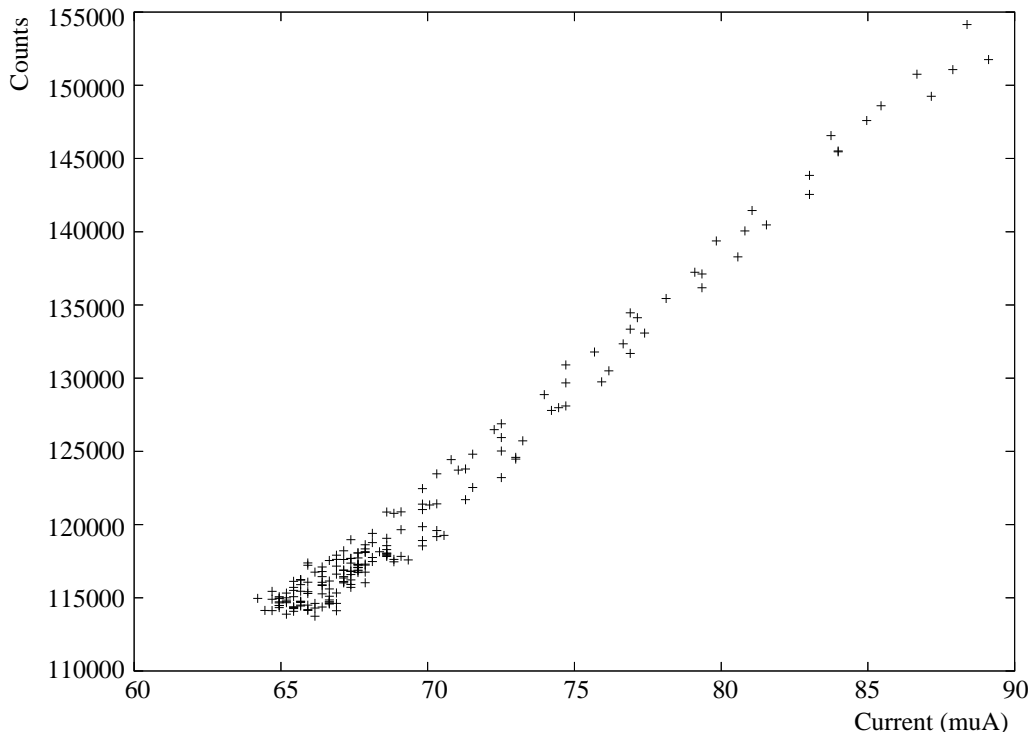


Figure 5.9: Total counts within 60 seconds as function of X-ray current.

rate within the detector shows a linear dependence on the tube current. In order to compensate for this, the current is logged before and after each measurement. Each measurement with an absorber in the beam is then scaled bin-wise with the quotient of the currents with and without absorber.

All spectra are then corrected for Compton scattering for energies below 9 keV. X-ray photons can be scattered inelastically within the collimator in front of the entry window and in the detector itself. This loss of energy outside the active volume of the detector deteriorates the spectrum and causes an increase in the spectrum at low energies.

In order to correct for this effect each spectrum is fitted with the sum of an exponential function and a polynomial function of second degree.

The polynomial function describes the decrease in intensity with decreasing energy of the bremsstrahlung spectrum, following the Rayleigh-Jeans law. The exponential

function describes the amount of Compton scattered photons per energy. Therefore, the Compton background can be eliminated by subtracting the exponential function. This works well for energies $\gtrsim 3$ keV. For very low energies the Backscatter effect becomes dominant. Additionally, the transmission function of the detector window can only be approximated as being fully transparent for energies > 1.5 keV. These limitations do not influence the measurements done, as the intensity of the spectrum is very low for energies ≤ 6 keV (see Figure 5.10), for these energies a determination of the transmission will not be possible due to the limited statistics of the data.

In order to obtain the relative absorption the spectra for the different absorber materials are divided bin-wise by a spectrum without absorber. In order to reduce the statistical error, the spectra can be rebinned.

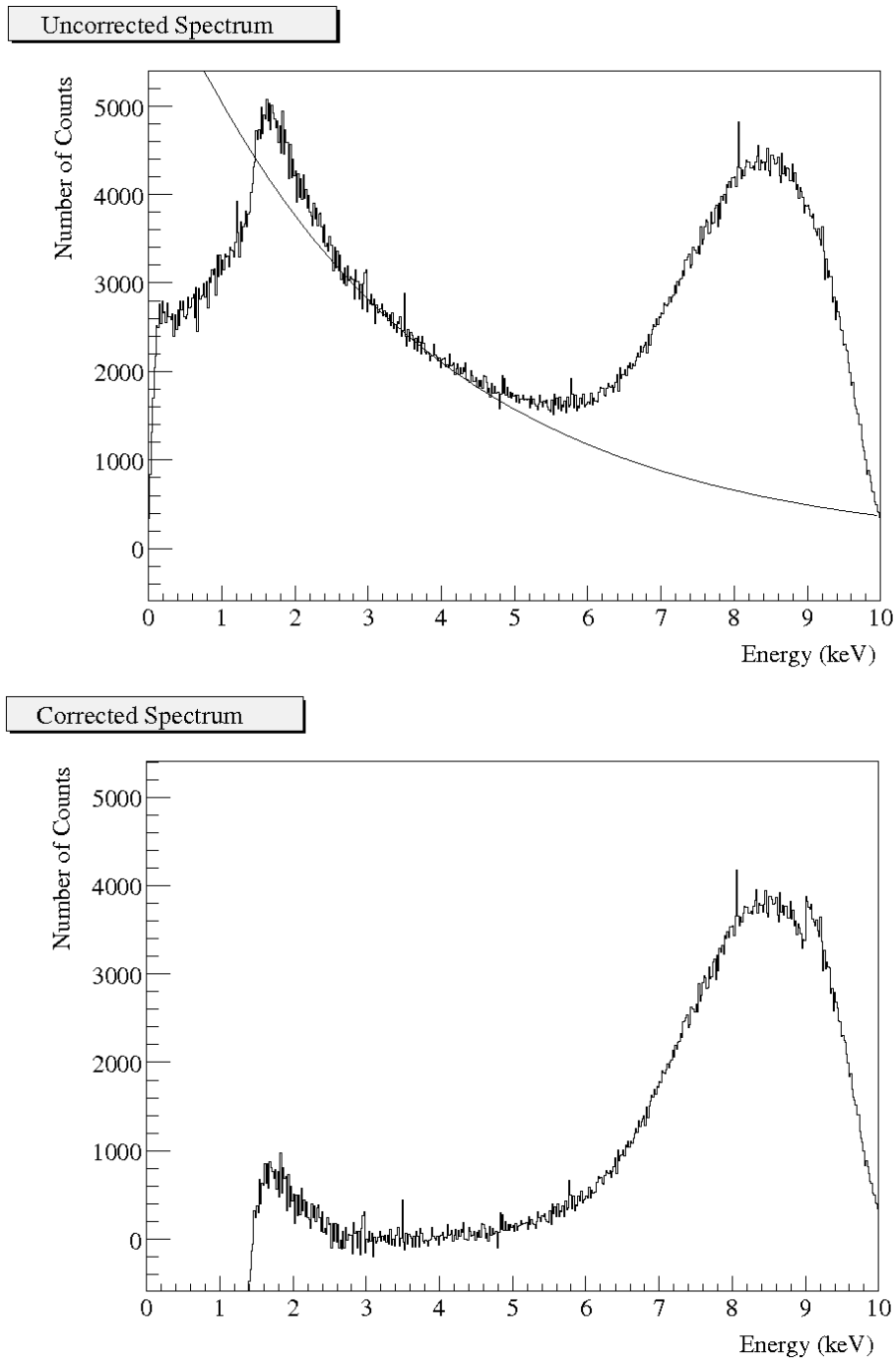


Figure 5.10: Example for a spectrum, the upper spectrum before, the lower after the Compton background has been subtracted

6. Quality Control Measurements and Analysis

In order to ensure a homogenous quality of the radiators built at Münster, the X-ray transmission of full radiators, cover plates, fibre mats and grid-bars was measured. The K_α -line of Copper at 8.04 keV was chosen as reference energy. This energy is near the maximum of the TR-spectrum at approximately 10 keV. It will also be easily available in the future - for example for possible measurements of replacement radiators produced later - as X-ray sources with a copper target are standard sources that are used at many physics facilities.

6.1 X-Ray Transmission of the Components

As described in chapter 3.2.2, the radiator consists of two cover plates which are spaced by a grid-like structure. The cells of this structure are filled with stacks of fibre mats. Samples of all of these components were available for measurements.

For each spectrum, data has been taken over a timespan of 200s. For the thicker absorbers, the bars and the stacks of seven mats, this time has been extended to 300s.

6.1.1 Cover Plates

X-ray Transmission of the Cover Plates

The transmission of X-rays through the cover plate has already been watched very carefully during the selection of the final materials for the radiator. [Buc05] The coating, though it is very thin, has a much higher density than the rest of the materials used in the radiator and should therefore contribute significantly to the absorption of X-rays within the full radiator. Radiographic measurements with an X-ray diffractometer at the *Chemisches Institut, Münster* using the Cu- K_α line on material samples from different manufacturers have supported this. The relative transmission of pure HF71 with 8 mm thickness is $\approx 70\%$, the coating contributes another 75 – 83%, depending on the manufacturer. This amounts to a relative transmission

of the full cover plate of 52 – 61%. Two important causes for this variation were identified: Different thicknesses of the carbon fibre mats and different amounts of the epoxy used for glueing.

The material that was finally chosen is produced by *Fischer Advanced Composite Components AG (FACC)*. The relative absorption of X-rays with 8.04 keV in the samples was $\approx 40\%$. In order to ensure this throughout the production process, samples of the cover plates used in the radiator production were also tested with the diffractometer of the *Chemisches Institut*, while the setup at the IKP was under construction. The plates of the first delivery had a mean transmission of 48.6% with a standard deviation of 1.97%. As this was significantly worse than the original sample. It turned out that FACC had increased the the amount of glue used in order to improve the properties of the surface.

As optimizing the X-ray transmission of the plates was a higher priority, the amount of glue was reduced, leading to an optimized transmission of $\approx 65\%$ in the following deliveries (see Figure 6.1).

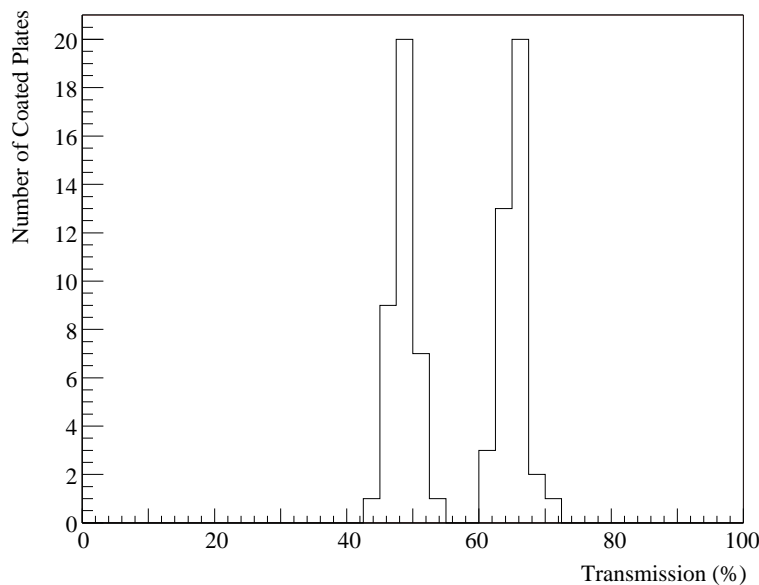


Figure 6.1: Absorption of all plates measured at the CI with an energy of 8.04keV

With the test stand described in Chapter 5 the absorption could be measured not only for samples but for full plates. Besides the measurements with the plates as

absorber, also measurements without an absorber were taken as reference value for the transmission. As can be seen in Figure 6.2, the values for the second delivery, measured at the *Chemisches Institut* is consistent with these measurement. As the first deliveries showed no large deviation of the transmission from the mean value within plates from the same delivery, only random samples of different sizes were chosen from the last deliveries. The transmission of a total number of 171 plates was measured. Except for the first delivery all covers that were measured are consistent with a mean transmission of 64.6% with a standard deviation of 2.9%. It could be

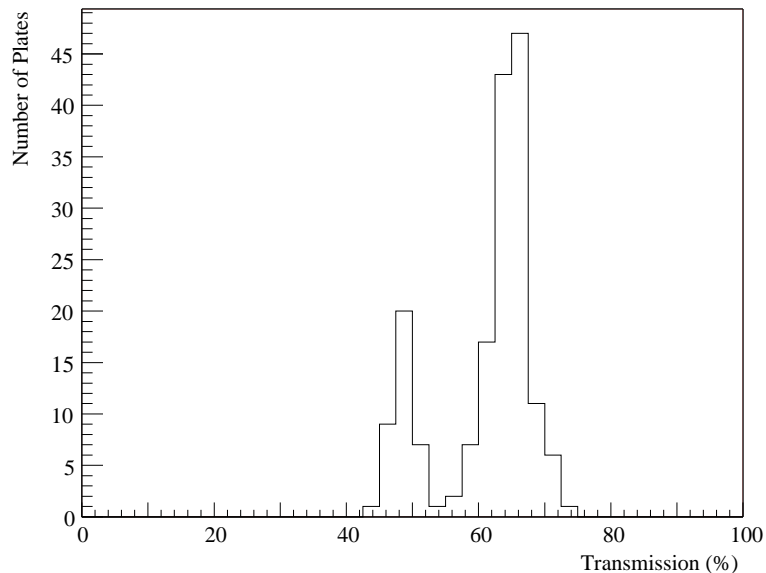


Figure 6.2: Absorption of all measured plates at 8.04keV. Measurements from the CI and IKP.

seen that the amount of glue used by FACC can be controlled very well by these measurements.

Statistical and Systematical Errors

The influence of systematic errors on the measurements is expected to be small, as not absolute count rates but their quotient is relevant, thereby cancelling out multiplicative effects. Through the fixed geometry of the test stand, comparable conditions are ensured for all measurements.

Environmental influences like changes in temperature or humidity influence the current of the X-ray generator, but due to the linearity between photon yield and current demonstrated in chapter 5.6 and the corrections implemented in the analysis, no impact on the results is expected.

In order to estimate the size of the systematic error of the measurements, one plate (number 177) was measured repeatedly on different days. 40 measurements were acquired for this plate over a period of 2.5 months. Due to the low statistics, a Gaussian fit could not be applied. The RMS value of the distribution of the transmission is 3.7% with a mean value of 65.7%. The mean statistical error of the single plate measurements at the IKP is 3.8 ± 0.1 . As the deviation of the transmission in the repeated plate measurement can be fully explained within the mean statistical error of the single measurement, the influence of possible systematic errors can be neglected.

For the calculation of the transmission at 8.04 keV only the channel that contains this energy is used. Although the response function of the detector is gaussian, this is possible, as the spectrum can be approximated as flat near the peak of the spectrum. Then the response functions cancel out¹, so that the count rate at 8.04 keV can be assumed to be the count rate without energy smearing of the detector.

Assuming no further error sources, the difference between the deviation predicted by the statistical error and the actual width of the distribution is likely being contributed by irregularities of the plates. An upper limit can be computed from Gaussian error propagation, the error is obtained by propagating the error of the statistical error. From

$$\sqrt{dT_{tot}^2 - dT_{stat}^2} = dT_{var} \quad (6.1)$$

with dT_{tot} being the total error for all plates and dT_{stat} the statistical error for the single measurement, the variation of the transmission of the plates, given by dT_{var} , can be calculated.

In the measurements made at the IKP no deviation beyond the statistical error can be seen.

The measurements made at the *Chemisches Institut* have better statistics, the mean value of the statistical error $0.43 \pm 0.05\%$. The distribution of these transmissions has

¹According to signal theory, the experimentally seen spectrum can be obtained from the ideal spectrum by folding it with a response function: $f_{exp}(x) = \int_{-\infty}^{\infty} f_{th}(y)f_R(x-y)dy$ with f_{exp} being a constant a and f_R being a Gauss function, the equation can be solved with $f_{th} = a$.

a standard deviation $\sigma = 1.8\%$, from Equation 6.1 the upper limit for the variation of the plates is calculated to be $1.65 \pm 0.05\%$.

Influence of the Coating on the Transmission

In order to estimate the contribution of the coating to the total absorption of the plate, the transmission of several cross bars was measured through their flat face. The bars are made from the same material as the cover plates with the same thickness. Only their length and width differ. At 8.04 keV a mean transmission of 72.1% with a standard deviation of 4.1% has been obtained from the measurement of 28 plates. With these data the transmission of the coating and the glue can be calculated. They contribute to the X-ray attenuation with a total transmission of $89.7 \pm 6.5\%$. For the first delivery, which had worse transmission properties, it is only $66.9 \pm 7.9\%$.

6.1.2 Bars

As mentioned above, the bars are made from the same material (*Rohacell HF71*) which is the basis for the cover plates. Nevertheless, the X-ray transmission through the side which is glued to the coverplates is measured to have a reference value for calculating the influence of the glue on the X-ray transmission within the full radiator at the bars of the grid structure within.

From Figure 6.3 the mean transmission has been determined to be 26.1% with a standard deviation of 3.1%.

6.1.3 Polypropylene Mats

Seven polypropylene mats are put in each cell of the radiator. Samples from several cut-sizes were examined for their absorption properties. The mean value for the transmission of a single mat is 89.5% with a standard deviation of 5.7%, calculated via RMS. The distribution of the transmission can be found in Figure 6.4. The deviation is wider than that of any of the other components. This can be explained with the random structure of the mats. Although the manufacturer ensured a good homogeneity of local thickness and density throughout each mat, these measurements hint at small local variations.

Therefore the mats were grouped into stacks of seven as in the radiator, to reduce these intrinsic, local fluctuations. The standard deviation is significantly smaller (see

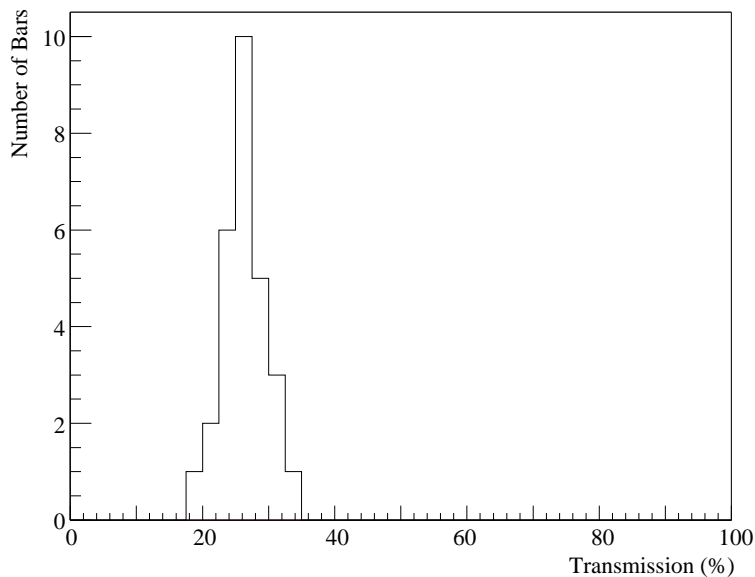


Figure 6.3: Transmission of the cross bars at 8.04keV

Figure 6.5). The mean transmission is $48.3 \pm 3.5\%$. Both values are consistent with each other within their respective errors.

6.2 X-ray Transmission of the Full Radiator

As demonstrated in the last section, the components of the radiator show no significant deviations. Thus it is expected that the full radiators show a similarly constant behavior.

The only difference in the measurements is that, for the most radiators, the reference measurement is no longer one without absorber. As the radiators have been packed in foil after assembly to protect them from dust and humidity, two layers of this foil are used as absorber for the reference measurement. The division the two spectra cancels out the absorption within the foil. Each spectrum has been taken over a period of time of 300s.

For all 223 tested radiators the X-ray transmission through one chamber in the support grid filled with fibre mats, is measured. The X-ray transmission of the chambers of the full radiator is 20.6% with a standard deviation of 2.4%. A small

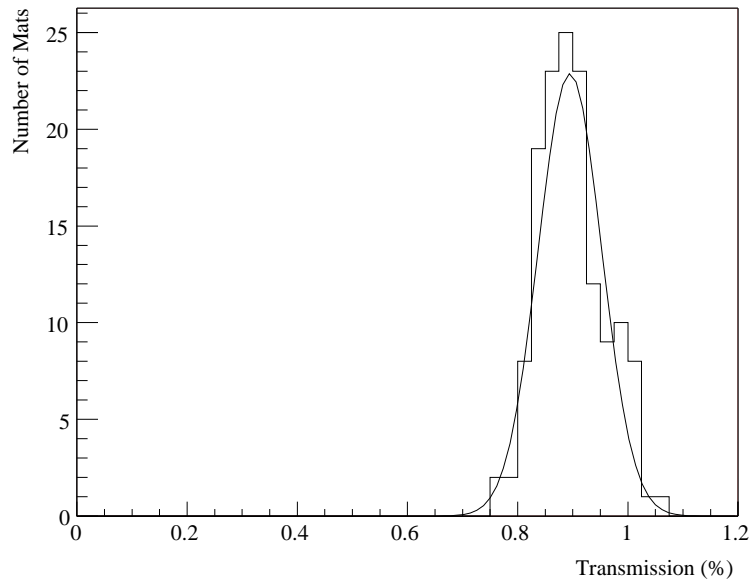


Figure 6.4: Transmission of the single mats at 8.04keV

number of radiators is not consistent with this and is excluded from the fit. These radiators have a mean transmission of only $7.99 \pm 2.63\%$. They are built from the first delivery of cover plates that has a reduced transmission (see Figure 6.6). From the measurements of the components, the transmission for two cover plates and a stack of seven mats was calculated to be $20.2 \pm 1.5\%$ and $11.4 \pm 1.1\%$. These values are consistent with the values actually measured.

For several radiators, the transmission of two chambers was measured. Comparing these two measurements of the same radiators by dividing the transmission of one chamber by the transmission of the other, yields the distribution displayed in Figure 6.7. The mean value is 1.00098. The standard deviation is 0.18 and can be understood from the standard deviation of the radiators.

The X-ray transmission is also measured for 89 radiators at the position of a bar of the grid-structure. The transmission here is $10.0 \pm 2.2\%$ 6.8. This values are obtained from a Gaussian fit to all entries below a transmission of 15%. As the bars are very slim, the other values, which are consistent with the value for the chambers, result from not having hit the bar with the beam. From the values of the component measurements a total transmission of 10.9 ± 1.4 is calculated. The transmission of the

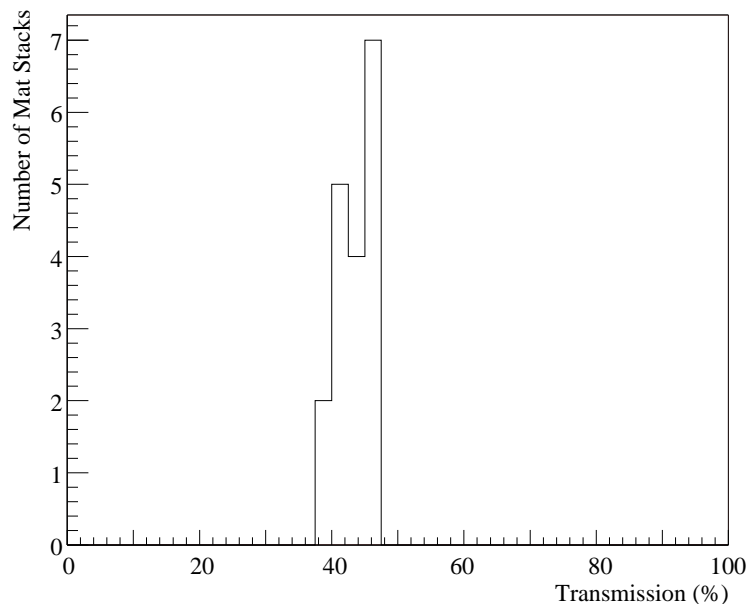


Figure 6.5: Transmission of the stack of 7 mats at 8.04keV

glue can be derived from this. The value obtained is 85.1% with an error, computed via error propagation, of 22.9%. This error does not mirror the distribution of the values, as the small error of the transmission of the full radiator suggests a very good homogeneity.

6.3 Results

In Table 6.1, the X-ray transmissions of the various absorbers are assembled, the values of the individual measurements are presented in appendix A. The variation of the transmission has been computed using Equation 6.1 and a one σ value of the errors for the total deviation and the statistical error of the single measurement. The values given can be regarded as an upper limit for the deviation. The transmission of the components varies generally by less than 3 absolute percent of the original transmission. One exception are the single fibre mats. The wide spread of the values has been explained with the irregularities of the mats. As the stacks of seven mats show only a variance similar to that of the other components, these differences seem to cancel out. The other exception is the first batch of cover plates, with a

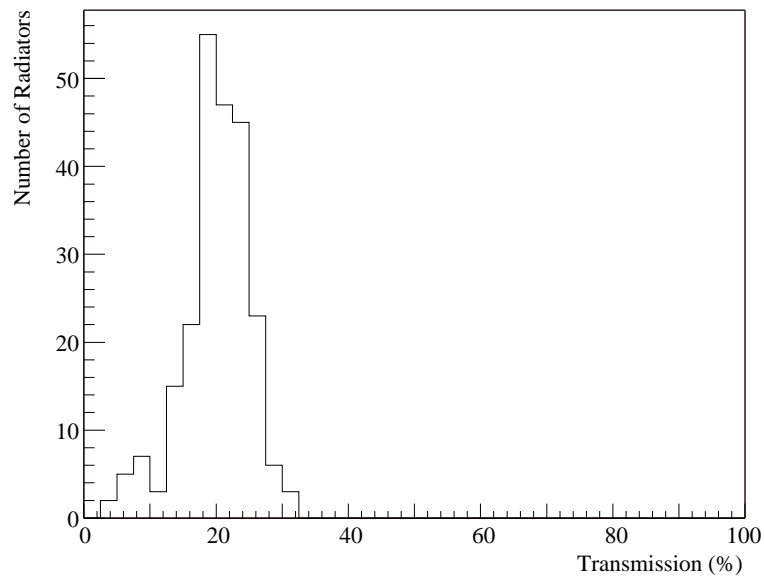


Figure 6.6: Transmission of the radiators through chamber at 8.04keV

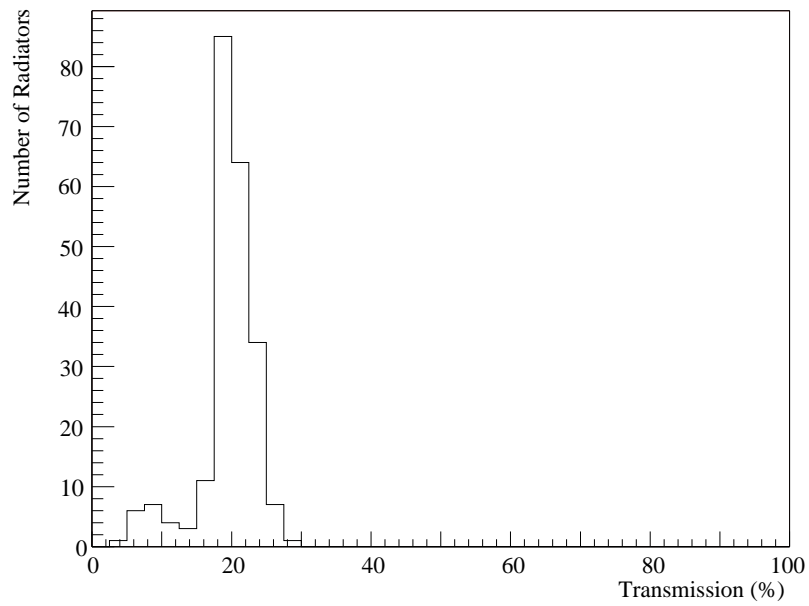


Figure 6.7: Division of the transmission of two chambers of the same radiator

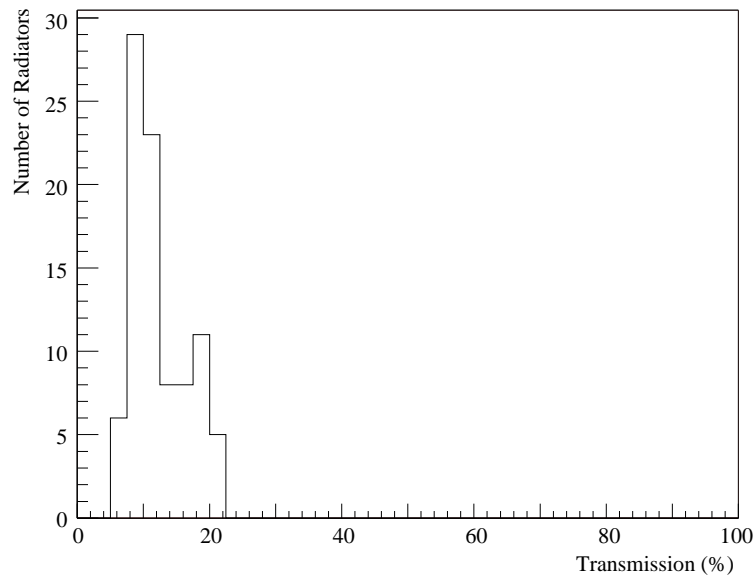


Figure 6.8: Transmission of the radiators through a bar at 8.04 keV

transmission $\approx 15\%$ worse than the following. The reasons could be identified and an improvement of the transmission, compared to that of the initial samples, resulted from this.

The variation in the transmission of the radiators is better than 2%, the improvement compared to the values of the components can be explained by the better statistics of these measurements.

The transmission of the glue and of the plate coating could be calculated from the acquired data.

| Absorber | Transmission in % | statistical error in % | variation of component in % |
|--------------------|----------------------|------------------------|--------------------------------|
| cover plates | 64.7 ± 2.9 | $<3.8 \pm 0.1$ | 1.7 ± 0.1 |
| pure HF71 plates | 72.1 ± 4.1 | 3.4 ± 0.1 | 2.3 ± 0.3 |
| cross bars | 26.1 ± 3.3 | 2.3 ± 0.2 | 2.4 ± 0.4 |
| single mat | 89.5 ± 5.7 | 6.6 ± 0.5 | 15.9 ± 0.4 |
| stack of 7 mats | 48.3 ± 3.5 | 2.0 ± 0.1 | 2.8 ± 0.1 |
| radiator/chamber | 20.6 ± 2.4 | 2.1 ± 0.1 | 1.2 ± 0.1 |
| radiator/cross-bar | 10.0 ± 2.2 | 1.2 ± 0.2 | 1.8 ± 0.3 |
| plate coating | 89.7 ± 6.5 | | |
| glue / cross-bar | 85.1 ± 22.9 | | |

Table 6.1: Transmission of components and full TRD for X-ray radiation with 8.04 keV

7. Parameterization of the Transmission Function

7.1 Parameterization of X-Ray Transmission

In this chapter the examination of the X-ray transmission of the radiators and their components is described with respect to their energy dependence. In measurements done at the University of Heidelberg on prototypes with discrete energies between 5.9 keV and 36.4 keV the radiator was nearly transparent for X-rays with energies $\gtrsim 20\text{keV}$. For lower energies the transmission decreased; at $\approx 6\text{keV}$, the radiator reached a transmission of ≈ 0 [Leh04].

The use of a bremsstrahlung source for the measurements described in this thesis makes it possible to determine the transmission of the radiator continuously for energies between $\approx 6 - 10$ keV. With the variable X-ray source described in Chapter 5.5.1, the energy range can be extended to 50.65 keV.

The data from the bremsstrahlung source is filled into a histogram. The bin width is 450 eV, in order to reduce the statistical error of the data points and to minimize distortions, especially near the steep rises in intensity of the spectra, due to the limited energy resolution. For the parameterization of the transmission, mean values for all components and radiators are used.

For the variable X-ray source, all counts within a 2σ interval of each peak are summed up in the individual spectra before calculating the transmission. Only for the K_β lines of Mo and Cu, the interval is reduced to 1σ , in order to exclude peripheral values of the peak, which are strongly influenced by background photons. For the Cu- and Rb-lines in the measurement of the full radiator at the cross bar, this value is decreased further to 0.5σ , due to the high attenuation in the radiator. The data points shown in the figures of this chapter are obtained from one sample of each component. The radiator measurements are carried out with a small radiator with only 3 full scale fibre mat chambers. It has been built for test purposes from materials identical to those used for the full scale radiators.

The errors are generally determined by the resolution capability of the detector and by statistical error. For the measurements with the discrete X-ray source, the

variation of each component according to Table 6.1 is added, to compensate the possible deviation of the sample from the mean value.

As discussed in chapter 4.2, the attenuation of X-rays in matter can be calculated from an exponential function using the density of the material ρ , its thickness x and the corresponding mass attenuation coefficient μ_m as parameters. The mass attenuation coefficient itself is a function of the X-ray energy and of the absorber material.

The exact description of photon attenuation is important for various applications, not only in physics, but also in chemistry, biology and medicine. Therefore, quantitative measurements of the attenuation of photons in matter have been carried out throughout the last century, the first measurements dating back to 1907. A comprehensive overview can be found in [Hub99]. Besides various tabulations (for example [Hub, Hen93]), numerous attempts have been made to give a parameterization dependant on the energy E and the element, characterized by its atomic number Z . Typically, these parameterizations are generated from fits to tabulated values of μ_m . In order to describe the energy dependent transmission of the radiator and the various components, different parameterizations of the mass attenuation coefficients were considered. Reasons for excluding parameterizations were a narrowly limited range of energy, where it is applicable (e.g. [Thi79]), the exclusion of chemical elements necessary for the fits (e.g. [Ger86]) or a great set of parameters necessary (e.g. [Mid04, Zsc89]). The work of Orlic et.al [Orl93] is valid for the energy range from 100 eV to 1000 keV. This allows an extrapolation of the transmission function to energies greater than 50 keV, where no measurements have been done so far. Furthermore, all elements from $Z = 1-92$ are included, whereas especially Hydrogen has often been excluded in other works. The parameterization bases upon the semi-empirical approach

$$\mu_m = e^{p_1+p_2(\ln \lambda)+p_3(\ln \lambda)^2+p_4(\ln \lambda)^3} + \sigma_{KN} \frac{ZN_A}{M}. \quad (7.1)$$

The Klein-Nishina cross section σ_{KN} ¹ describes the contribution of incoherent scattering, Z being the atomic number of the respective element, M its atomic weight

¹The Klein-Nishina cross section σ_{KN} is given by

$$\sigma_{KN} = 2\pi r_e^2 \left(\frac{1+k}{k^2} \left(\frac{2(1+k)}{1+2k} - \frac{\ln(1+2k)}{k} \right) + \frac{\ln(1+2k)}{2k} - \frac{1+3k}{(1+2k)^2} \right)$$

with $k = E/(mc^2)$ and $mc^2 = 511.0034$ keV and the electron radius $r = 2.817939 \cdot 10^{-13}$ cm. The energy E is given in keV.

and N_A the Avogadro number. The contribution of other effects (see Equation 4.2) is parameterized with a polynomial of third degree. A set of parameters is valid between two adjacent absorption edges. As the energies used are significantly larger than the energy of the K -edge of the light elements, which is smaller than 1 eV, only one set of parameters is needed for each element. The radiator is made from different compounds consisting of Oxygen, Carbon, Hydrogen and Nitrogen. The parameters can be found in Table 7.1.

| Z | Symbol | p_1 | p_2 | p_3 | p_4 |
|-----|--------|----------|---------|---------|-----------|
| 1 | H | -6.48071 | 3.27538 | 0.04385 | - 0.00866 |
| 6 | C | 0.11476 | 3.09245 | 0.03213 | -0.02494 |
| 7 | N | 0.63927 | 3.08731 | 0.01587 | -0.02538 |
| 8 | O | 1.08730 | 3.07389 | 0.00035 | -0.02438 |

Table 7.1: Parameters p_1 - p_4 for energies $E > E_K$ according to [Orl93]

The error in the energy range from 5 – 100 keV given by Orlic et.al. is 1 – 2%.

7.2 Mats

The fibre mats of the TRD are made of polypropylene (C_3H_6). According to Equation 4.3, the resulting mass attenuation coefficient μ_m can be written as:

$$\mu_m = 3 \frac{m_C}{N_A} \mu_{m,C} + 6 \frac{m_H}{N_A} \mu_{m,H}. \quad (7.2)$$

The density ρ of the mats is 0.074 g/cm³, the thickness of a full stack is 3.2 cm. The transmission function calculated from these values describes the measured data well within their errors, as displayed in Figure 7.1.

7.3 Rohacell HF71

The plates and bars of the radiator are made from *Rohacell HF71*, which is a poly-methacrylimid (5· H, 3· C, 1· O, 1· N). The calculation of the mass attenuation for these components from the equation above, gives a good description of the data (see Figure 7.2). The density of *Rohacell HF71* is 0.075 g/cm³, the thickness of the plates is 0.8 cm.

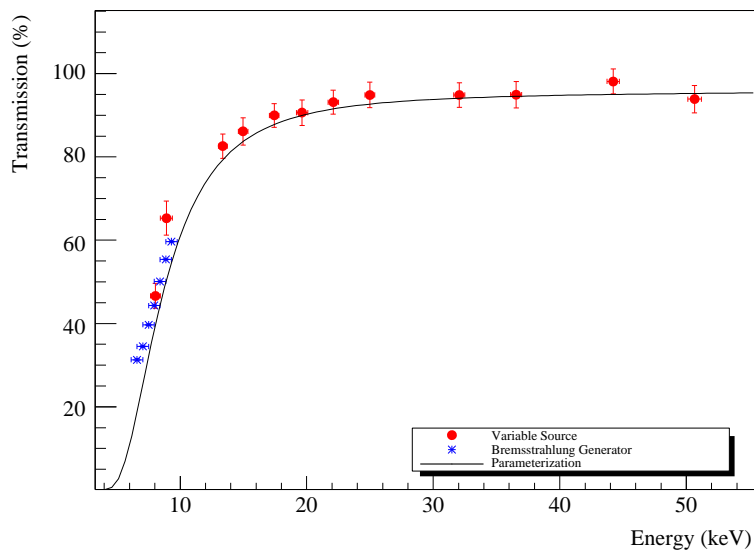


Figure 7.1: Transmission function of a 7 mat stack

The cross-bars of the grid are made from the same material, but with a thickness of 3.2 cm. The parameterization is in good agreement with the measured data (see Figure 7.3).

7.4 Cover Plates

While the basic component of the cover plates, *Rohacell HF71*, could be described easily, the carbon coating is not open for such a direct parameterization, as especially the exact amount of the glue used is not known. The dominant element in this coating is Carbon. Therefore, the transmission function of the coating can be approximated, assuming it consists of pure Carbon, the thin aluminium coating of the foil glued to the plate is neglected in this approximation.

At 8.04 keV the mean value of the transmission of the coating is 90.1 % (see Table 6.1). From Equation 7.1 we can calculate $\mu_m(8.04 \text{ keV}) = 4.49 \text{ cm}^2/\text{g}$. Together with Equation 4.1, this facilitates the calculation of the effective mass m_{eff} of the coating:

$$\ln \left(\frac{I}{I_0} \right) \frac{1}{-\mu} = \rho x = m_{eff}. \quad (7.3)$$

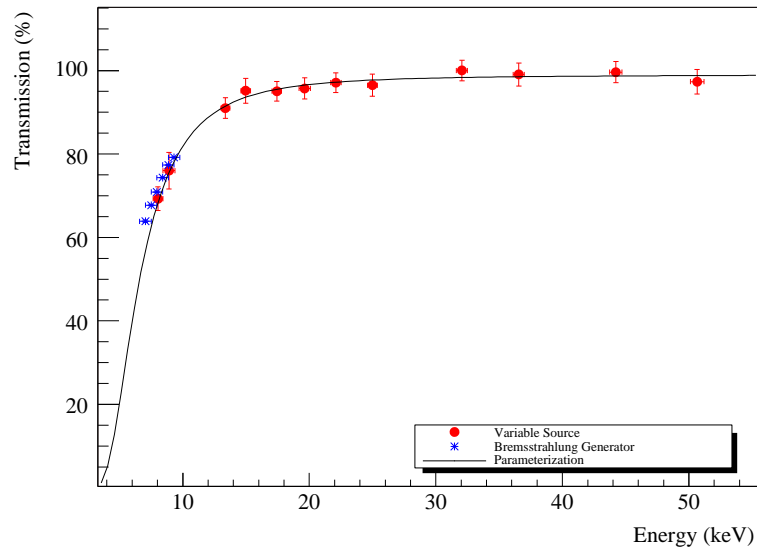


Figure 7.2: Transmission function of the pure *Rohacell* plates

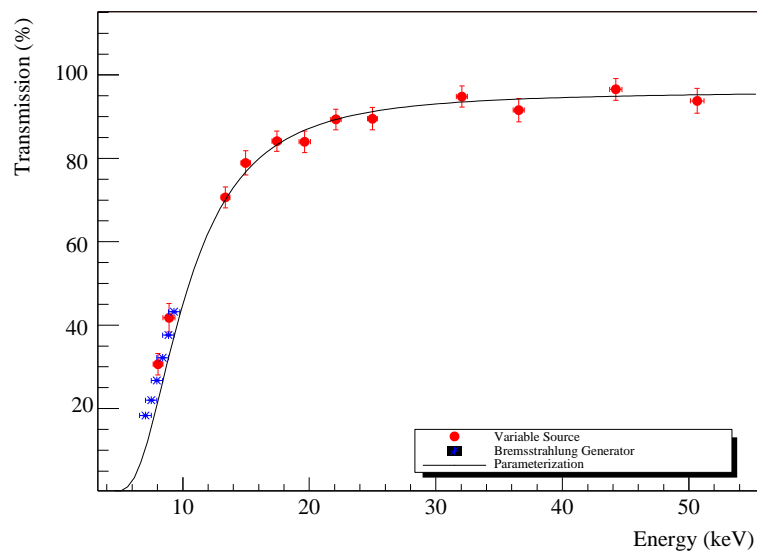


Figure 7.3: Transmission function of the cross bars

With the values above we obtain: $m_{eff} = 0.0242 \text{ g/cm}^2$. With this value we can calculate the energy transmission of the coating as a function of the incident photon energy. Multiplying this transmission with the function of the pure *Rohacell HF71* plates yields a good description of the measured transmissions of the plates (see Figure 7.4).

7.5 Full Radiator

The transmission of the fibre-mat chambers of the complete radiator can be computed by multiplying the individual transmissions for two plates and one stack of seven mats. As shown in Figure 7.5, the data is described very well.

In order to compute the transmission of the radiator at the crossbars the transmission of the glue has to be computed. We make use of the same approximation as for the cover plates, but instead of pure Carbon, we use the chemical composition of epoxide for the calculation (4· H, 2· C, 1· H). The transmission of the glue at 8.04 keV is 84.5 % (see Table 6.1), with $\mu_m(8.04 \text{ keV}) = 7.88913 \text{ cm}^2/\text{g}$ the value $m_{\text{eff,g}} = 0.0292 \text{ g/cm}^2$ for the effective mass is obtained. The transmission function shown in Figure 7.6 is derived from the multiplication of the transmissions of two plates and one bar together with that of the glue, computed from the values above.

It is in good agreement with the measured values, only the data points obtained with the Cu and Rb targets deviate significantly. These are the targets with the smallest photon yield.

The transmission function of the radiators as well as of the components used can be described very well with a semi-empirical parametrization of the mass attenuation coefficient. With the simple assumptions that were made, as the exact chemical composition of, for example the *Rohacell HF71*, is unknown, due to legal restrictions, the energy dependency of the transmission for the various materials and radiators could be described well.

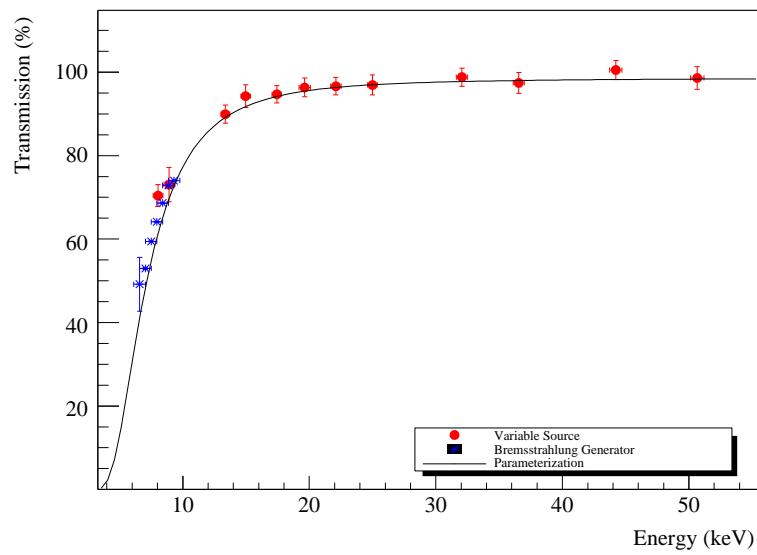


Figure 7.4: Transmission function of the cover plates

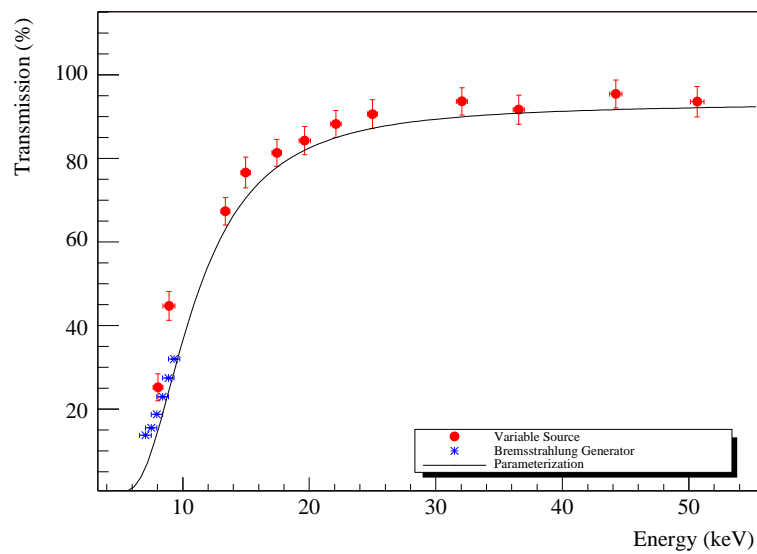


Figure 7.5: Transmission function of the full radiator at a fibre mat chamber

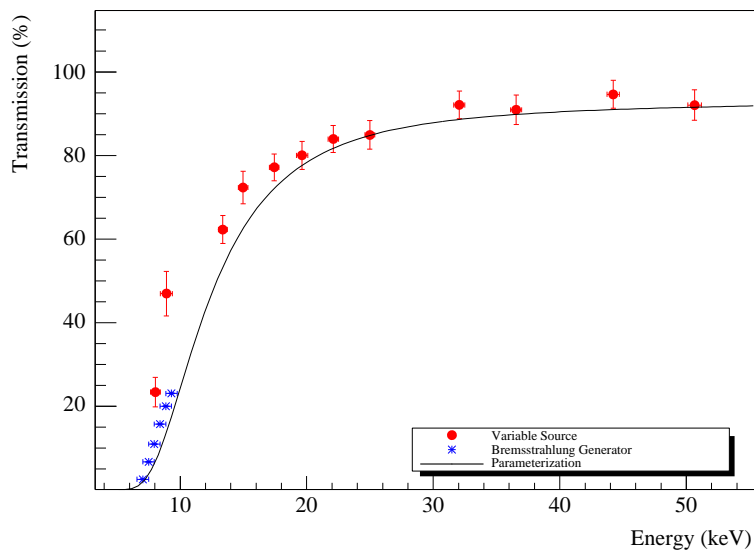


Figure 7.6: Transmission function of the full radiator at a cross bar

7.6 Influence of the Transmission on the Gas Gain

For the small radiator, with 3 cells of polypropylene fibre mats, the X-ray transmission was measured at intervals over the full length. As can be seen in Figure 7.7 the transmissions are very well compatible with the mean transmission of the chambers and bars, derived from the measurements of all radiators. The position of the bars is sharply determined.

A similar behaviour can be observed, when the gas gain of a TRD module is measured in small steps over one dimension of the module. The gas is ionized by X-rays from a generator identical to the one described in chapter 5.3.1. It is operated at a higher current, but at a lower voltage $U_{\max} = -8$ kV (see Figure 7.8) [Fre05].

Dividing the gain at the bar position by the gain at the chamber yields a factor of 0.4 ± 0.05 .

As a reference value the expected transmission, the parameterizations for the transmission of the radiator at a fibre mat chamber and at a bar are integrated over the energy in the interval from 7.0 keV to 8.0 keV, as the radiator is still transparent

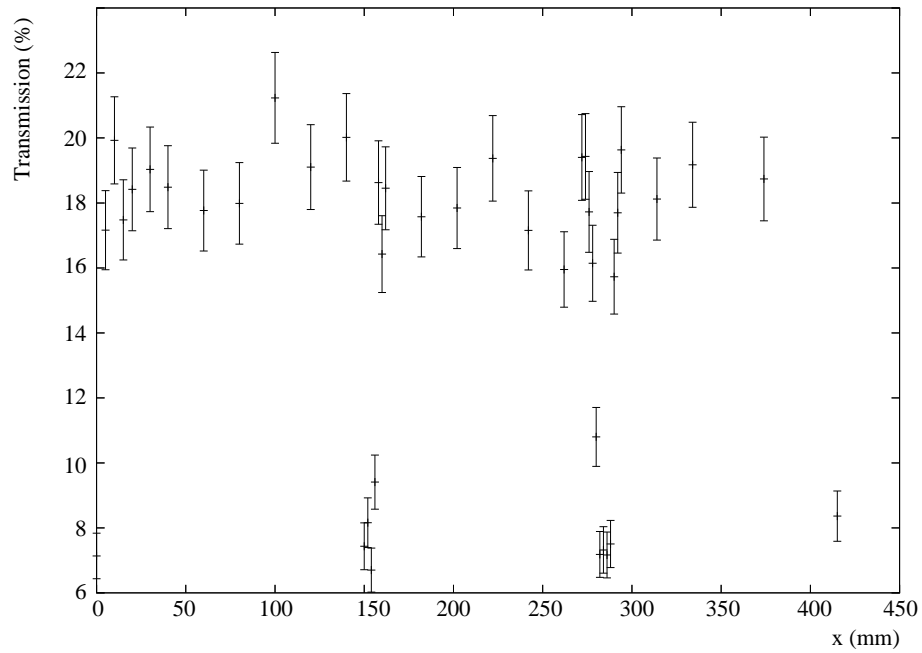


Figure 7.7: Plot of X-ray transmission as function of location

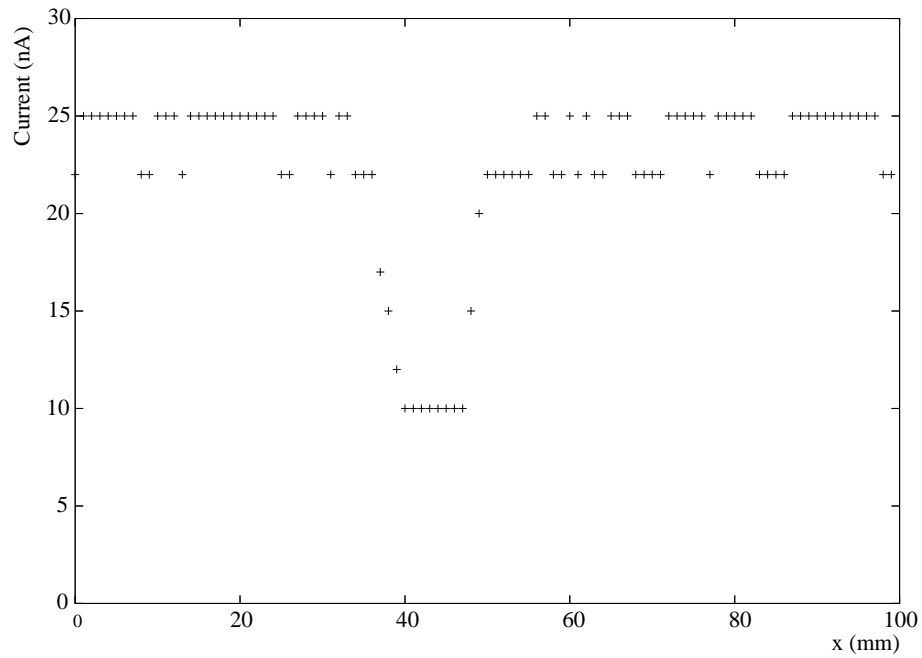


Figure 7.8: Gain measurement of a full TRD module [Fre05]

at these energies. The ratio of the two values is 0.39 ± 0.03 , which is in very good agreement with the measured value.

8. Summary

In this thesis the transmission function of radiators for the ALICE-TRD regarding X-ray photons has been examined.

For the measurements a test stand, based on a bremsstrahlung X-ray source and a Si(Li) detector with good energy resolution, was developed. A detailed overview over the mechanics, the electronics and the software including the Labview based DAQ and control software, is given.

The transmission at 8.04 keV has been chosen as a benchmark value for the various components and for the complete radiators, the mean transmission of each has been determined. For the complete radiators it is $20.6\% \pm 2.4\%$.

For the components, the overall variation of the transmission has been determined to be less than 3%, for the radiator the upper limit is 3.2%. The transmission of the glue and the plate coating could not be measured directly and has been calculated from the obtained data.

The energy dependence of the X-ray transmission has been studied. The transmission measurements taken with the bremsstrahlung source up to 10 keV were extended up to 50 keV with discrete energies.

A semi-empirical parameterization of the X-ray transmission has been compared to the data. The components and the full radiators are in good agreement with the parameterization. A transmission function for the plate coating and the glue has been determined, using the values obtained at 8.04 keV.

Predictions derived from the parameterization for the difference in transmission between the radiator chambers and the radiator at the cross-bars were compared to the measured reduction of the observed charge in gas gain measurements at the position of the cross-bars. The results are in good agreement.

A. Data Tables

Table A.1: Transmission of all radiators at 8.04 keV

| Radiator | Transmission | Radiator | Transmission |
|----------|--------------------|----------|--------------------|
| L1C1-01 | 21.95% \pm 2.07% | L1C1-12 | 19.96% \pm 1.91% |
| L1C1-02 | 17.11% \pm 1.79% | L1C1-13 | 18.23% \pm 1.81% |
| L1C1-03 | 18.11% \pm 1.85% | L1C1-14 | 21.39% \pm 1.99% |
| L1C1-04 | 21.16% \pm 2.02% | L1C1-15 | 22.66% \pm 2.05% |
| L1C1-05 | 19.4% \pm 1.88% | L1C1-16 | 17.99% \pm 1.79% |
| L1C1-06 | 19.47% \pm 1.93% | L1C1-17 | 19.87% \pm 1.93% |
| L1C1-07 | 22.39% \pm 2.04% | L1C1-18 | 23.95% \pm 2.16% |
| L1C1-08 | 20.85% \pm 1.96% | L1C1-19 | 12.33% \pm 1.41% |
| L1C1-09 | 20.15% \pm 1.92% | L1C1-20 | 11% \pm 1.32% |
| L1C1-10 | 19.43% \pm 1.92% | L1C1-21 | 11.44% \pm 1.35% |
| L1C1-11 | 17.64% \pm 1.77% | | |
| L2C0-10 | 20.92% \pm 1.4% | L2C0-14 | 19.44% \pm 1.4% |
| L2C0-11 | 18.33% \pm 1.3% | L2C0-15 | 19.02% \pm 1.38% |
| L2C0-12 | 19.08% \pm 1.33% | L2C0-17 | 19.98% \pm 1.42% |
| L2C0-13 | 14.91% \pm 1.15% | L2C0-18 | 22.17% \pm 1.57% |
| L2C1-01 | 23.16% \pm 2.18% | L2C1-19 | 17.09% \pm 1.26% |
| L2C1-02 | 22.79% \pm 2.07% | L2C1-20 | 18.73% \pm 1.32% |
| L2C1-03 | 22.56% \pm 2.06% | L2C1-21 | 19.98% \pm 1.38% |
| L2C1-04 | 20.79% \pm 1.96% | L2C1-22 | 18.48% \pm 1.34% |
| L2C1-05 | 24.35% \pm 2.11% | L2C1-23 | 17.8% \pm 1.31% |
| L2C1-06 | 19.85% \pm 1.87% | L2C1-24 | 20.3% \pm 1.41% |
| L2C1-07 | 19.09% \pm 1.85% | L2C1-25 | 19.61% \pm 1.38% |
| L2C1-08 | 20.97% \pm 1.96% | L2C1-26 | 20.78% \pm 1.51% |

Continued on next page

Table A.1: Transmission of all radiators at 8.04 keV

| Radiator | Transmission | Radiator | Transmission |
|----------|--------------------|----------|--------------------|
| L2C1-09 | 21.73% \pm 1.98% | L2C1-27 | 17.75% \pm 1.3% |
| L2C1-10 | 20.98% \pm 1.96% | L2C1-28 | 19.63% \pm 1.46% |
| L2C1-11 | 21.03% \pm 1.94% | L2C1-29 | 20.51% \pm 1.49% |
| L2C1-12 | 21.59% \pm 1.99% | L2C1-30 | 19.09% \pm 1.43% |
| L2C1-13 | 21.97% \pm 2% | L2C1-31 | 20.66% \pm 1.5% |
| L2C1-14 | 21.78% \pm 1.99% | L2C1-32 | 17.98% \pm 1.32% |
| L2C1-15 | 23.37% \pm 2.07% | L2C1-33 | 19.42% \pm 1.38% |
| L2C1-16 | 24.56% \pm 2.13% | L2C1-34 | 18.64% \pm 1.4% |
| L2C1-17 | 21.42% \pm 1.97% | L2C1-35 | 16.9% \pm 1.32% |
| L2C1-18 | 20.38% \pm 1.91% | L2C1-36 | 15.96% \pm 1.28% |
| L3C0-01 | 18.58% \pm 1.59% | L3C0-10 | 22.53% \pm 1.86% |
| L3C0-02 | 20.56% \pm 1.68% | L3C0-11 | 20.53% \pm 1.76% |
| L3C0-03 | 22.04% \pm 1.75% | L3C0-12 | 23.09% \pm 1.82% |
| L3C0-04 | 22.32% \pm 1.76% | L3C0-13 | 19.89% \pm 1.67% |
| L3C0-05 | 22.76% \pm 1.87% | L3C0-14 | 21.56% \pm 1.86% |
| L3C0-06 | 20.16% \pm 1.93% | L3C0-15 | 21.58% \pm 1.75% |
| L3C0-07 | 19.89% \pm 1.65% | L3C0-16 | 19.44% \pm 1.75% |
| L3C0-08 | 18.88% \pm 1.35% | L3C0-17 | 22.95% \pm 1.93% |
| L3C0-09 | 21.88% \pm 1.82% | L3C0-18 | 28.98% \pm 2.22% |
| L3C1-01 | 19.89% \pm 1.88% | L3C1-19 | 17.93% \pm 1.87% |
| L3C1-02 | 22.96% \pm 2.05% | L3C1-20 | 19.53% \pm 1.9% |
| L3C1-03 | 25.94% \pm 2.33% | L3C1-21 | 21.79% \pm 2.02% |
| L3C1-04 | 16.51% \pm 1.39% | L3C1-22 | 23.01% \pm 2.09% |
| L3C1-05 | 18.79% \pm 1.93% | L3C1-23 | 23.02% \pm 2.17% |
| L3C1-06 | 26.26% \pm 2.35% | L3C1-24 | 21.46% \pm 2.01% |
| L3C1-07 | 23.5% \pm 2.2% | L3C1-25 | 19.03% \pm 1.27% |

Continued on next page

Table A.1: Transmission of all radiators at 8.04 keV

| Radiator | Transmission | Radiator | Transmission |
|----------|--------------------|----------|--------------------|
| L3C1-08 | 22.52% \pm 2.14% | L3C1-27 | 17.62% \pm 1.21% |
| L3C1-09 | 13.91% \pm 1.06% | L3C1-28 | 17.6% \pm 1.21% |
| L3C1-10 | 23.56% \pm 2.2% | L3C1-29 | 21.2% \pm 1.37% |
| L3C1-11 | 23.46% \pm 2.19% | L3C1-30 | 20.16% \pm 1.33% |
| L3C1-12 | 22.61% \pm 2.15% | L3C1-31 | 20.01% \pm 1.29% |
| L3C1-13 | 23.16% \pm 1.89% | L3C1-32 | 18.47% \pm 1.23% |
| L3C1-14 | 20.92% \pm 1.78% | L3C1-33 | 17.95% \pm 1.21% |
| L3C1-15 | 20.75% \pm 1.77% | L3C1-34 | 19.85% \pm 1.29% |
| L3C1-16 | 26.6% \pm 2.05% | L3C1-35 | 17.81% \pm 1.22% |
| L3C1-17 | 18.88% \pm 1.63% | L3C1-36 | 20.35% \pm 1.32% |
| L3C1-18 | 19.92% \pm 1.73% | | |
| L4C0-01 | 18.86% \pm 1.41% | L4C0-10 | 15.86% \pm 1.22% |
| L4C0-02 | 16.84% \pm 1.32% | L4C0-11 | 18.66% \pm 1.34% |
| L4C0-03 | 18.27% \pm 1.32% | L4C0-12 | 27.41% \pm 2.18% |
| L4C0-04 | 20.37% \pm 1.41% | L4C0-13 | 20.28% \pm 1.47% |
| L4C0-05 | 19.63% \pm 1.44% | L4C0-14 | 22.8% \pm 1.57% |
| L4C0-06 | 20.75% \pm 1.85% | L4C0-15 | 21.7% \pm 1.53% |
| L4C0-07 | 25.43% \pm 2.08% | L4C0-16 | 19.86% \pm 1.45% |
| L4C0-08 | 19.21% \pm 1.36% | L4C0-17 | 19.65% \pm 1.44% |
| L4C0-09 | 22.94% \pm 1.96% | L4C0-18 | 18.06% \pm 1.37% |
| L4C1-01 | 20.06% \pm 1.89% | L4C1-20 | 18.55% \pm 1.24% |
| L4C1-02 | 23.41% \pm 2.07% | L4C1-21 | 22.63% \pm 1.48% |
| L4C1-03 | 26.16% \pm 2.15% | L4C1-22 | 22.55% \pm 1.47% |
| L4C1-04 | 20.26% \pm 1.84% | L4C1-23 | 18.79% \pm 1.23% |
| L4C1-05 | 21.65% \pm 1.92% | L4C1-24 | 20.24% \pm 1.38% |
| L4C1-06 | 21.51% \pm 1.91% | L4C1-25 | 19.03% \pm 1.24% |

Continued on next page

Table A.1: Transmission of all radiators at 8.04 keV

| Radiator | Transmission | Radiator | Transmission |
|----------|--------------------|----------|--------------------|
| L4C1-07 | 21.53% \pm 1.91% | L4C1-26 | 18.99% \pm 1.29% |
| L4C1-08 | 22.3% \pm 1.95% | L4C1-27 | 18.71% \pm 1.28% |
| L4C1-09 | 19.36% \pm 1.8% | L4C1-28 | 19.78% \pm 1.41% |
| L4C1-11 | 24.28% \pm 2.27% | L4C1-29 | 18.39% \pm 1.27% |
| L4C1-12 | 24.94% \pm 2.31% | L4C1-30 | 18.26% \pm 1.35% |
| L4C1-13 | 23.65% \pm 2.23% | L4C1-31 | 19.07% \pm 1.24% |
| L4C1-14 | 23.19% \pm 2.21% | L4C1-32 | 19.84% \pm 1.29% |
| L4C1-15 | 22.73% \pm 2.18% | L4C1-33 | 21.42% \pm 1.35% |
| L4C1-16 | 27.28% \pm 2.43% | L4C1-34 | 21.04% \pm 1.49% |
| L4C1-17 | 24.48% \pm 2.28% | L4C1-35 | 19.44% \pm 1.42% |
| L4C1-18 | 22.15% \pm 2.15% | L4C1-36 | 14.84% \pm 1.13% |
| L4C1-19 | 19.59% \pm 1.28% | | |
| L5C1-01 | 18.86% \pm 1.53% | L5C1-19 | 18.53% \pm 1.26% |
| L5C1-02 | 21.94% \pm 1.43% | L5C1-20 | 18.89% \pm 1.27% |
| L5C1-03 | 21.69% \pm 1.42% | L5C1-21 | 18.5% \pm 1.29% |
| L5C1-04 | 21.74% \pm 1.43% | L5C1-22 | 17.1% \pm 1.2% |
| L5C1-05 | 20.91% \pm 1.39% | L5C1-23 | 20.79% \pm 1.38% |
| L5C1-06 | 19.73% \pm 1.34% | L5C1-25 | 20.55% \pm 1.37% |
| L5C1-07 | 23.31% \pm 1.49% | L5C1-26 | 20.25% \pm 1.36% |
| L5C1-08 | 20.1% \pm 1.35% | L5C1-27 | 19.91% \pm 1.31% |
| L5C1-09 | 22.17% \pm 1.43% | L5C1-28 | 17.66% \pm 1.22% |
| L5C1-10 | 17.02% \pm 1.24% | L5C1-29 | 18.92% \pm 1.27% |
| L5C1-11 | 19.37% \pm 1.34% | L5C1-30 | 16.76% \pm 1.19% |
| L5C1-12 | 19.2% \pm 1.33% | L5C1-31 | 19.18% \pm 1.28% |
| L5C1-13 | 18.82% \pm 1.31% | L5C1-32 | 21.96% \pm 1.53% |
| L5C1-14 | 18.08% \pm 1.28% | L5C1-33 | 19.61% \pm 1.43% |

Continued on next page

Table A.1: Transmission of all radiators at 8.04 keV

| Radiator | Transmission | Radiator | Transmission |
|----------|--------------------|----------|--------------------|
| L5C1-15 | 18.14% \pm 1.29% | L5C1-34 | 15.96% \pm 1.27% |
| L5C1-16 | 20.44% \pm 1.36% | L5C1-35 | 19.95% \pm 1.44% |
| L5C1-17 | 19.08% \pm 1.31% | L5C1-36 | 21.3% \pm 1.5% |
| L5C1-18 | 19.92% \pm 1.34% | | |
| L6C1-01 | 7.64% \pm 0.93% | L6C1-10 | 8.93% \pm 1.02% |
| L6C1-02 | 5.51% \pm 0.78% | L6C1-11 | 4.16% \pm 0.69% |
| L6C1-03 | 8.46% \pm 0.98% | L6C1-12 | 5.51% \pm 0.8% |
| L6C1-04 | 6.53% \pm 0.9% | L6C1-13 | 6.28% \pm 0.86% |
| L6C1-05 | 5.77% \pm 0.84% | L6C1-14 | 8.28% \pm 1% |
| L6C1-06 | 7.99% \pm 1% | L6C1-15 | 9.2% \pm 1.05% |
| L6C1-07 | 6.5% \pm 0.9% | L6C1-35 | 19.79% \pm 1.34% |
| L6C1-08 | 11.73% \pm 1.23% | L6C1-36 | 23.68% \pm 1.55% |
| L6C1-09 | 7.98% \pm 0.96% | | |

Table A.2: Transmission of all radiators at a cross-bar at 8.04 keV

| Radiator | Transmission | Radiator | Transmission |
|----------|--------------------|----------|--------------------|
| L2C0-10 | 17% \pm 1,52% | L2C1-24 | 10,89% \pm 1,21% |
| L2C0-11 | 20,75% \pm 1,71% | L2C1-25 | 8,33% \pm 1,05% |
| L2C0-12 | 19,92% \pm 1,67% | L2C1-26 | 7,66% \pm 1,06% |
| L2C0-13 | 12,84% \pm 1,3% | L2C1-27 | 8,5% \pm 1,06% |
| L2C0-14 | 18,58% \pm 1,67% | L2C1-28 | 7,8% \pm 1,07% |
| L2C0-15 | 20,91% \pm 1,79% | L2C1-29 | 17,66% \pm 1,68% |
| L2C0-16 | 17,64% \pm 1,62% | L2C1-30 | 7,31% \pm 1,03% |
| L2C0-17 | 18,24% \pm 1,65% | L2C1-31 | 8,9% \pm 1,15% |
| L2C0-18 | 8% \pm 1,14% | L2C1-32 | 7,79% \pm 1,02% |
| L2C1-19 | 8,04% \pm 1,01% | L2C1-33 | 12,86% \pm 1,34% |
| L2C1-20 | 9,28% \pm 1,1% | L2C1-34 | 6,65% \pm 0,97% |
| L2C1-21 | 10,08% \pm 1,15% | L2C1-35 | 12,67% \pm 1,38% |
| L2C1-22 | 17,73% \pm 1,6% | L2C1-36 | 9,27% \pm 1,16% |
| L2C1-23 | 7,78% \pm 1,02% | | |
| L3C0-08 | 12,8% \pm 1,32% | | |
| L3C1-09 | 14,07% \pm 1,31% | L3C1-31 | 9,87% \pm 1,06% |
| L3C1-25 | 17,92% \pm 1,5% | L3C1-32 | 9,08% \pm 1,02% |
| L3C1-26 | 17,23% \pm 1,49% | L3C1-33 | 18,37% \pm 1,5% |
| L3C1-27 | 19,67% \pm 1,58% | L3C1-34 | 16,31% \pm 1,41% |
| L3C1-28 | 11,11% \pm 1,15% | L3C1-35 | 10,91% \pm 1,13% |
| L3C1-29 | 19,64% \pm 1,61% | L3C1-36 | 14,82% \pm 1,34% |
| L3C1-30 | 17,37% \pm 1,5% | | |
| L4C0-03 | 10,4% \pm 1,18% | L4C0-10 | 10,78% \pm 1,2% |
| L4C0-04 | 13,99% \pm 1,39% | L4C0-11 | 9,2% \pm 1,1% |
| L4C0-08 | 7,22% \pm 0,97% | | |

Continued on next page

Table A.2: Transmission of all radiators at a cross-bar at 8.04 keV

| Radiator | Transmission | Radiator | Transmission |
|----------|--------------------|----------|--------------------|
| L4C1-19 | 19,28% \pm 1,56% | L4C1-28 | 21,85% \pm 1,84% |
| L4C1-20 | 8,7% \pm 1% | L4C1-29 | 13,28% \pm 1,29% |
| L4C1-21 | 21,46% \pm 1,75% | L4C1-30 | 11,17% \pm 1,25% |
| L4C1-22 | 11,05% \pm 1,2% | L4C1-31 | 17,38% \pm 1,44% |
| L4C1-23 | 15,44% \pm 1,34% | L4C1-32 | 15,5% \pm 1,37% |
| L4C1-24 | 8,76% \pm 1,06% | L4C1-33 | 8,71% \pm 1% |
| L4C1-25 | 10,02% \pm 1,06% | L4C1-34 | 8,98% \pm 1,13% |
| L4C1-26 | 7,43% \pm 0,94% | L4C1-35 | 9,85% \pm 1,19% |
| L4C1-27 | 7,03% \pm 0,91% | L4C1-36 | 10,54% \pm 1,15% |
| L5C1-10 | 7,82% \pm 0,99% | L5C1-23 | 12,1% \pm 1,24% |
| L5C1-11 | 11,74% \pm 1,23% | L5C1-25 | 7,85% \pm 0,98% |
| L5C1-12 | 9,76% \pm 1,11% | L5C1-26 | 12,09% \pm 1,24% |
| L5C1-13 | 7,89% \pm 0,99% | L5C1-27 | 10,45% \pm 1,12% |
| L5C1-14 | 8,05% \pm 1% | L5C1-28 | 7,01% \pm 0,9% |
| L5C1-15 | 10,56% \pm 1,16% | L5C1-29 | 10,39% \pm 1,11% |
| L5C1-16 | 9,8% \pm 1,1% | L5C1-30 | 17,03% \pm 1,47% |
| L5C1-17 | 11,69% \pm 1,22% | L5C1-31 | 10,21% \pm 1,1% |
| L5C1-18 | 10,35% \pm 1,14% | L5C1-32 | 12,43% \pm 1,35% |
| L5C1-19 | 10,18% \pm 1,1% | L5C1-33 | 9,99% \pm 1,2% |
| L5C1-20 | 22,37% \pm 1,72% | L5C1-34 | 10,32% \pm 1,22% |
| L5C1-21 | 7,9% \pm 0,98% | L5C1-35 | 10,3% \pm 1,22% |
| L5C1-22 | 8,27% \pm 0,98% | L5C1-36 | 7,71% \pm 1,04% |

Table A.3: Transmission of all cover plates at 8.04 keV

| Cover Plate | Transmission | Cover Plate | Transmission |
|-------------|--------------------|-------------|--------------------|
| 1 | 47,91% \pm 0,41% | 139 | 66,43% \pm 3,95% |
| 2 | 50,47% \pm 0,42% | 140 | 65,73% \pm 3,92% |
| 3 | 47,21% \pm 0,4% | 141 | 67,5% \pm 3,95% |
| 4 | 48,84% \pm 0,41% | 142 | 64,18% \pm 3,82% |
| 5 | 48,6% \pm 0,41% | 143 | 66,39% \pm 3,91% |
| 6 | 48,37% \pm 0,41% | 144 | 61,13% \pm 3,69% |
| 7 | 47,91% \pm 0,41% | 145 | 65,15% \pm 3,86% |
| 8 | 51,16% \pm 0,42% | 146 | 67,5% \pm 3,95% |
| 9 | 47,44% \pm 0,4% | 147 | 63,21% \pm 3,83% |
| 10 | 47,67% \pm 0,4% | 148 | 63,92% \pm 3,86% |
| 11 | 46,6% \pm 0,41% | 149 | 57,1% \pm 3,57% |
| 12 | 49,51% \pm 0,42% | 150 | 63,72% \pm 3,76% |
| 13 | 53,4% \pm 0,45% | 151 | 61,55% \pm 3,68% |
| 14 | 48,3% \pm 0,42% | 152 | 57,47% \pm 3,51% |
| 15 | 48,06% \pm 0,42% | 153 | 66,66% \pm 3,7% |
| 16 | 51,94% \pm 0,44% | 154 | 64,18% \pm 3,6% |
| 17 | 51,94% \pm 0,44% | 155 | 63,61% \pm 3,58% |
| 18 | 49,76% \pm 0,43% | 156 | 69,13% \pm 3,79% |
| 19 | 47,57% \pm 0,41% | 157 | 60,13% \pm 3,44% |
| 20 | 50% \pm 0,43% | 158 | 65,53% \pm 3,18% |
| 21 | 46,6% \pm 0,41% | 159 | 66,27% \pm 3,21% |
| 22 | 44,66% \pm 0,4% | 160 | 63,06% \pm 3,19% |
| 23 | 46,6% \pm 0,41% | 161 | 58,93% \pm 3% |
| 24 | 48,06% \pm 0,42% | 162 | 59,48% \pm 3,02% |
| 25 | 48,79% \pm 0,42% | 163 | 64,63% \pm 3,37% |
| 26 | 48,3% \pm 0,42% | 165 | 65,54% \pm 3,2% |

Continued on next page

Table A.3: Transmission of all cover plates at 8.04 keV

| Cover Plate | Transmission | Cover Plate | Transmission |
|-------------|--------------------|-------------|--------------------|
| 27 | 48,54% \pm 0,42% | 166 | 64,74% \pm 3,18% |
| 28 | 46,12% \pm 0,4% | 167 | 69,49% \pm 3,34% |
| 29 | 45,61% \pm 0,4% | 168 | 65,38% \pm 3,17% |
| 30 | 47,07% \pm 0,41% | 169 | 63,35% \pm 3,14% |
| 31 | 49,27% \pm 0,42% | 170 | 66,9% \pm 3,26% |
| 32 | 46,6% \pm 0,41% | 171 | 64,04% \pm 3,16% |
| 34 | 52,44% \pm 0,44% | 172 | 65,63% \pm 3,21% |
| 35 | 49,27% \pm 0,42% | 173 | 64,04% \pm 3,15% |
| 36 | 49,76% \pm 0,43% | 174 | 65,74% \pm 3,21% |
| 37 | 47,56% \pm 0,41% | 175 | 66,38% \pm 3,2% |
| 38 | 51,22% \pm 0,43% | 176 | 60,11% \pm 2,99% |
| 39 | 49,02% \pm 0,42% | 177 | 69,99% \pm 3,87% |
| 43 | 60,49% \pm 0,49% | 178 | 69,47% \pm 3,85% |
| 44 | 62,2% \pm 0,5% | 179 | 67,41% \pm 3,77% |
| 45 | 64,63% \pm 0,51% | 180 | 65,84% \pm 3,71% |
| 46 | 70% \pm 0,54% | 181 | 70,18% \pm 3,88% |
| 47 | 64,63% \pm 0,51% | 182 | 70,03% \pm 3,87% |
| 48 | 63,9% \pm 0,51% | 183 | 65,59% \pm 3,7% |
| 49 | 65,37% \pm 0,51% | 184 | 66,71% \pm 3,71% |
| 50 | 63,17% \pm 0,5% | 185 | 62,24% \pm 3,54% |
| 51 | 64,63% \pm 0,51% | 186 | 64,14% \pm 3,61% |
| 52 | 65,37% \pm 0,51% | 187 | 67,4% \pm 3,77% |
| 53 | 64,15% \pm 0,51% | 188 | 63,93% \pm 3,63% |
| 54 | 65,12% \pm 0,51% | 189 | 61,61% \pm 3,54% |
| 55 | 66,83% \pm 0,52% | 190 | 63,3% \pm 3,61% |
| 56 | 65,12% \pm 0,51% | 191 | 64,32% \pm 3,65% |

Continued on next page

Table A.3: Transmission of all cover plates at 8.04 keV

| Cover Plate | Transmission | Cover Plate | Transmission |
|-------------|--------------------|-------------|--------------------|
| 57 | 66,59% \pm 0,52% | 192 | 66,42% \pm 3,73% |
| 58 | 66,59% \pm 0,52% | 193 | 68,01% \pm 3,79% |
| 59 | 68,54% \pm 0,53% | 194 | 59,42% \pm 3,45% |
| 60 | 65,85% \pm 0,52% | 195 | 62,88% \pm 3,59% |
| 61 | 66,99% \pm 0,52% | 196 | 61,72% \pm 3,54% |
| 62 | 64,1% \pm 0,5% | 197 | 62,53% \pm 3,5% |
| 63 | 62,41% \pm 0,49% | 198 | 60,89% \pm 3,44% |
| 64 | 67,23% \pm 0,52% | 199 | 65,56% \pm 3,62% |
| 65 | 66,27% \pm 0,52% | 200 | 64,57% \pm 3,58% |
| 66 | 62,65% \pm 0,5% | 201 | 66,72% \pm 3,6% |
| 67 | 63,61% \pm 0,5% | 202 | 62,98% \pm 3,46% |
| 68 | 67,32% \pm 0,52% | 203 | 61,65% \pm 3,41% |
| 70 | 65,54% \pm 0,51% | 204 | 63,01% \pm 3,53% |
| 71 | 71,08% \pm 0,54% | 205 | 67,76% \pm 3,72% |
| 72 | 65,54% \pm 0,51% | 206 | 64,32% \pm 3,59% |
| 73 | 65,54% \pm 0,51% | 207 | 64,08% \pm 3,58% |
| 74 | 66,27% \pm 0,52% | 208 | 61,81% \pm 3,61% |
| 75 | 65,78% \pm 0,51% | 209 | 70,76% \pm 3,97% |
| 76 | 66,34% \pm 0,52% | 210 | 68,64% \pm 3,89% |
| 77 | 64,1% \pm 0,5% | 211 | 64,77% \pm 3,73% |
| 78 | 66,75% \pm 0,52% | 212 | 72,72% \pm 4,05% |
| 79 | 62,89% \pm 0,5% | 213 | 63,16% \pm 3,67% |
| 80 | 64,58% \pm 0,51% | 214 | 61,24% \pm 3,55% |
| 81 | 63,86% \pm 0,5% | 215 | 68,23% \pm 3,83% |
| 129 | 65,35% \pm 3,77% | 216 | 65,5% \pm 3,72% |
| 130 | 69,57% \pm 3,94% | 217 | 61,28% \pm 3,55% |

Continued on next page

Table A.3: Transmission of all cover plates at 8.04 keV

| Cover Plate | Transmission | Cover Plate | Transmission |
|-------------|--------------------|-------------|--------------------|
| 131 | 70,32% \pm 3,97% | 218 | 63,07% \pm 3,62% |
| 132 | 62,93% \pm 3,68% | 219 | 60,9% \pm 3,58% |
| 133 | 59,5% \pm 3,54% | 220 | 70,23% \pm 3,91% |
| 134 | 58,18% \pm 3,48% | 221 | 67,33% \pm 3,63% |
| 135 | 58,13% \pm 3,61% | 222 | 64,48% \pm 3,52% |
| 136 | 62,94% \pm 3,81% | 223 | 66,19% \pm 3,67% |
| 137 | 59,55% \pm 3,67% | 224 | 64,62% \pm 3,61% |
| 138 | 61,95% \pm 3,77% | | |

Table A.4: Transmission of all mat stacks at 8.04 keV

| Mat Stack | Transmission |
|-----------|--------------------|
| L1C1-1 | 45,9% \pm 1,79% |
| L1C1-2 | 43,03% \pm 1,72% |
| L2C1-1 | 47,31% \pm 1,83% |
| L2C1-2 | 45,3% \pm 1,78% |
| L3C0-1 | 43,02% \pm 1,68% |
| L3C0-2 | 41,11% \pm 1,63% |
| L3C1-1 | 43,63% \pm 1,7% |
| L3C1-2 | 47,57% \pm 1,83% |
| L4C0-1 | 47,2% \pm 1,82% |
| L4C0-2 | 47,11% \pm 1,82% |
| L4C1-1 | 47,27% \pm 1,83% |
| L4C1-2 | 48,91% \pm 1,87% |
| L5C1-1 | 40,25% \pm 1,61% |
| L5C1-2 | 42,04% \pm 1,66% |
| L6C0-1 | 41,53% \pm 1,65% |
| L6C0-2 | 42,71% \pm 1,68% |
| L6C1-1 | 46,92% \pm 1,78% |
| L6C1-2 | 44,32% \pm 1,72% |

Table A.5: Transmission of all pure *Rohacell HF71* plates
at 8.04 keV

| Mat Stack | Transmission | Mat Stack | Transmission |
|-----------|--------------------|-----------|--------------------|
| 1 | 72,57% \pm 3,01% | 15 | 68,15% \pm 3,04% |
| 2 | 68,82% \pm 2,9% | 16 | 75,6% \pm 3,27% |
| 3 | 63,87% \pm 2,75% | 17 | 75,53% \pm 3,27% |
| 4 | 69,24% \pm 2,91% | 18 | 77,69% \pm 3,33% |
| 5 | 67,16% \pm 2,85% | 19 | 69,48% \pm 3,08% |
| 6 | 66,68% \pm 2,84% | 20 | 69,62% \pm 3,08% |
| 7 | 70,79% \pm 2,96% | 21 | 73,36% \pm 3,2% |
| 8 | 70,37% \pm 2,95% | 22 | 72,3% \pm 3,17% |
| 9 | 70,22% \pm 2,94% | 23 | 76,24% \pm 3,29% |
| 10 | 72,78% \pm 3,02% | 24 | 75,53% \pm 3,27% |
| 11 | 66,43% \pm 2,83% | 25 | 73,09% \pm 3,19% |
| 12 | 62,97% \pm 2,73% | 26 | 77,56% \pm 3,33% |
| 13 | 70,58% \pm 2,95% | 27 | 74,29% \pm 3,23% |
| 14 | 68,28% \pm 2,89% | 28 | 75,38% \pm 3,26% |

Table A.6: Transmission of all cross-bar samples at 8.04 keV

| Sample | Transmission | | | Sample | Transmission | | |
|--------|--------------|---|-------|--------|--------------|---|-------|
| L2-01 | 27% | % | 1,9% | L4-06 | 25,9% | % | 1,78% |
| L2-02 | 25,49% | % | 1,84% | L5-01 | 26,26% | % | 1,87% |
| L2-03 | 27,75% | % | 1,94% | L5-02 | 28,11% | % | 1,95% |
| L3-01 | 22,01% | % | 1,67% | L5-03 | 25,29% | % | 1,79% |
| L3-02 | 19,95% | % | 1,57% | L5-04 | 29,71% | % | 1,97% |
| L3-03 | 23,52% | % | 1,73% | L5-05 | 26,63% | % | 1,84% |
| L3-04 | 23,94% | % | 1,75% | L5-06 | 27,03% | % | 1,91% |
| L3-05 | 28,33% | % | 1,94% | L5-07 | 30,17% | % | 2,04% |
| L3-06 | 25,94% | % | 1,91% | L5-08 | 27,5% | % | 1,93% |
| L4-01 | 32,54% | % | 2,12% | L5-09 | 34,65% | % | 2,22% |
| L4-02 | 29,79% | % | 2,01% | L5-10 | 31,74% | % | 2,1% |
| L4-03 | 25,5% | % | 1,77% | L5-11 | 28,12% | % | 1,95% |
| L4-04 | 30,75% | % | 1,98% | L5-12 | 28,92% | % | 1,97% |
| L4-05 | 26,73% | % | 1,82% | L5-13 | 30,24% | % | 2,02% |

Bibliography

- [Ale02] Alessandro, B. et al. ALICE Physics: Theoretical Overview. 2002. CERN-ALICE-INTERNAL-NOTE-2002-025.
- [ALI95] ALICE: Technical proposal for a large ion collider experiment at the CERN LHC. 1995. CERN-LHCC-95-71.
- [And04] Andronic, A. and Braun-Munzinger, P. Ultrarelativistic nucleus-nucleus collisions and the quark- gluon plasma. 2004. [hep-ph/0402291](#).
- [Art75] Artru, X., Yodh, G., and Mennessier, G. Practical theory of the multilayered transition radiation detector. *Phys. Rev. D*, 12(5), pages 1289–1306, 1975.
- [Ava03] Avati, V. et al. The TOTEM experiment. *Eur. Phys. J. direct*, C34, page S255, 2003.
- [BM99] Braun-Munzinger, P. Physics of ultra-relativistic nuclear collisions with heavy beams at LHC energy. *Nucl. Phys.*, A661, pages 261–271, 1999. [nucl-ex/9908007](#).
- [BM00] Braun-Munzinger, P. and Stachel, J. (Non)thermal aspects of charmonium production and a new look at J/psi suppression. *Phys. Lett.*, B490, pages 196–202, 2000. [nucl-th/0007059](#).
- [Buc05] Bucher, D. IKP, Münster, personal communication, 2005.
- [Bus04] Busch, O. et al. Transition radiation spectroscopy with prototypes of the ALICE TRD. *Nucl. Instrum. Meth.*, A522, page 45, 2004. [physics/0404106](#).
- [CER99] AC Team, CERN Document Server, 1999. <http://cdsweb.cern.ch>, CERN-AC-9906026.

- [Cor02] Cortese, P. et al. ALICE: Addendum to the technical design report of the time of flight system (TOF). 2002. CERN-LHCC-2002-016.
- [Del00] Dellacasa, G. et al. ALICE technical design report of the Time Projection Chamber. 2000. CERN-OPEN-2000-183.
- [Dol93] Dolgoshein, B. Transition radiation detectors. *Nucl. Instr. and Meth.*, (A326), pages 434–469, 1993.
- [Ell04] Ellis, J. Physics at the LHC. *Eur. Phys. J.*, C34, pages 51–56, 2004.
- [Ems04] Emschermann, D. ALICE TRD in Heidelberg - Padplane, 2004. <http://www.physi.uni-heidelberg.de/demscher/alice/padplane/>.
- [Fre05] Freuen, S. Universität Heidelberg, personal communication. 2005.
- [Gar58] Garibian, G. Contribution to the theory of transition radiation. *Soviet Physics JETP*, 6(6), pages 1079–1085, 1958. Translation of: J. Exptl. Theoret. Phys. (U.S.S.R) 33, 1403-1410, 1957.
- [Gar60] Garibian, G. Transition radiation effects in particle energy losses. *Soviet Physics JETP*, 37(2), pages 372–376, 1960. Translation of: J. Exptl. Theoret. Phys. (U.S.S.R) 37, 527-533, 1959.
- [Ged72] Gedcke, D. The Si(Li) X-Ray Energy Analysis System: Operating principles and performance. *X-Ray Spect.*, 1, 1972.
- [Ger86] Gerward, L. Empirical Absorption Equations for use in X-ray spectrometric analysis. *X-ray spect.*, 15, pages 29–33, 1986.
- [Ger93] Gerward, L. X-ray attenuation coefficients: Current state of knowledge and availability. *Radiat. Phys. Chem.*, 41(4/5), pages 783–789, 1993.
- [Gin45] Ginzburg, V. and Frank, I. Radiation of a uniformly moving electron due to its transition from one medium into another. *Journal of Physics, Moscow*, 9(5), pages 353–362, 1945.
- [Giu01] Giubellino, P. and Crescio, E. The ALICE experiment at LHC: Physics prospects and detector design. 2001. CERN-ALICE-PUB-2000-035.
- [Giu02] Giubellino, P. Status of the ALICE experiment. *Eur. Phys. J. direct*, C4S1, page 05, 2002.

- [Giu04] Giubellino, P. Perspectives of the ALICE experiment. *Braz. J. Phys.*, 34, pages 166–169, 2004.
- [Hen93] Henke, B., Gullikson, E., and Davis, J. X-ray interactions: photoabsorption, scattering, transmission and reflection at $E=50\text{-}30000\text{eV}$, $Z=1\text{-}92$. *At. Data Nucl. Data Tables*, 54, pages 181–342, 1993.
- [Hub] Hubbell, J. and Seltzer, S. Tables of X-Ray Mass Attenuation Coefficients and Mass Energy-Absorption Coefficients. <http://physics.nist.gov/xaamdi>.
- [Hub99] Hubbell, J. Review of photon interaction cross section data in the medical and biological context. *Phys. med. Biol.*, 44, pages R1–R22, 1999.
- [Kno99] Knoll, G. F. *Radiation detection and measurement*. John Wiley & Sons, Inc., 3rd edition, 1999.
- [Leh04] Lehmann, T. *Vorbereitungen für die Qualitätstests der ALICE-TRD Kammer*. Diplomarbeit, Physikalisches Institut der Universität Heidelberg, 2004.
- [Leo87] Leo, W. *Techniques for Nuclear and Particle Physics Experiments*. Springer-Verlag, 1987.
- [LHC95] The Large Hadron Collider: Conceptual design. 1995. CERN-AC-95-05-LHC.
- [Lin04] Lindenstruth, V. and Musa, L. Fast on-detector integrated signal processing status and perspectives. *Nucl. Instr. and Meth.*, A522, pages 33–39, 2004.
- [Lud03] Ludlam, T. and McLerran, L. What have we learned from the Relativistic Heavy Ion Collider? *Phys. Today*, 56N10, pages 48–54, 2003.
- [Mid04] Midgley, S. A parametrization scheme for the x-ray linear absorption attenuation coefficient and energy absorption coefficient. *Phys. Med. Biol.*, 49, pages 307–325, 2004.
- [Orl93] Orlic, I., et al. Parametrization of the total photon mass attenuation coefficients in the energy range 0.1-1000 keV. *Nucl. Instr. and Meth.*, B74, pages 352–361, 1993.

- [Pai02] Paic, G. Heavy-ion physics at LHC. *Nucl. Phys.*, A699, pages 114–123, 2002.
- [PHO99] ALICE, Technical Design Report of the Photon Spectrometer (PHOS). 1999. CERN-LHCC-99-004.
- [ROO04] ROOT. ROOT System Home Page, 2004. <http://root.cern.ch>.
- [Sch02] Schmidt, H. Status and prospects of the CERN-LHC experiment ALICE. *Acta Physica Polonica B*, 33(6), pages 1651–1670, 2002.
- [Tar02] Tartarelli, G. F. Prospects for B physics with the ATLAS and CMS detectors. *Eur. Phys. J. direct*, C4S1, page 35, 2002.
- [Thi79] Thinh, T. P. and Leroux, J. New Basic Empirical expression for computing tables of X-ray mass attenuation coefficients. *X-ray Spect.*, 8(2), pages 85–91, 1979.
- [Tho01] Thompson, A. C. et al. *X-ray data booklet*. Lawrence Berkeley National Laboratory, 2001.
- [TRD99] A Transition Radiation Detector for electron identification within the ALICE central detector, Addendum to ALICE proposal. 1999. CERN-LHCC-99-013.
- [TRD01] Technical Design Report of the Transition Radiation Detector. 2001. CERN-LHCC-2001-021.
- [TRD05] ALICE TRD Website, 2005. <http://www-alice.gsi.de/trd/>.
- [Ver04] Verhoeven, W. IKP, Münster, personal communication, 2004.
- [Wom97] Womersley, J. The LHC physics program. 1997. To be published in the proceedings of 20th International Workshop on Fundamental Problems of High-Energy Physics and Field Theory, Protvino, Russia 24-26 Jun 1997.
- [Won94] Wong, C. *Introduction to High-Energy Heavy-Ion Collisions*. World Scientific, 1994.
- [Yur03] Yurevich, V. JINR, personal communication. 2003.
- [Zsc89] Zschornack, G. *Atomdaten für die Röntgenspektroanalyse*. Deutscher Verlag für die Grundstoffindustrie, 1. Auflage, 1989.

Danksagung

An dieser Stelle möchte ich mich bei allen bedanken, die zum Gelingen dieser Arbeit beigetragen haben.

Herrn Prof. Dr. Johannes P. Wessels danke ich für die interessante Aufgabenstellung und die hervorragenden Arbeitsbedingungen, vor allem aber für die Ermöglichung des interessanten und lehrreichen Aufenthaltes am CERN sowie der Teilnahme an zahlreichen Konferenzen und Tagungen. Prof. Dr. Rainer Santo danke ich für die freundliche Aufnahme am IKP und für die Vermittlung der Arbeitsgruppe.

Für die Betreuung meiner Arbeit und die zahlreichen Anregungen und Gespräche, die sehr zum Gelingen dieser Arbeit beigetragen haben, möchte ich Dr. Damian Bucher danken.

Dr. Klaus Reygers danke ich für die ständige Diskussionsbereitschaft und die Beantwortung vieler Fragen.

Wolfgang Verhoeven danke ich für seine große Unterstützung bei der Entwicklung des Aufbaus und bei der Durchführung der Messungen. Ausserdem gilt mein Dank Helmut Baumeister, Michael Balgenort, Roland Berendes, Norbert Heine und Hans-Werner Ortjohann für die Hilfe bei verschiedenen technischen Fragestellungen.

Für die gute Atmosphäre in der Arbeitsgruppe danke ich besonders Holger Gottschlag, sowie H.-H. Adam, J. Auffenberg, D. Emschermann, Dr. R. Glasow, J.F. Grosse-Oetringhaus, M. Hoppe, PD Dr. A. Khokaz, Dr. C. Klein-Bösing, T. Mersmann, T. Rausmann, B. Sahlmüller, A. Wilk und O. Zaudtke.

Für die kritische Durchsicht dieser Arbeit und die hilfreichen Anregungen möchte ich mich bei Dr. D. Bucher, Dr. C. Klein-Bösing, Dr. K. Reygers und A. Wilk bedanken. Bei meinen Eltern und vor allem bei Anna bedanke ich mich für die Unterstützung in allen Phasen meines Physikstudiums.

Eigenständigkeitserklärung

Ich versichere, diese Arbeit selbständig verfasst und keine anderen als die angegebenen Hilfsmittel und Quellen benutzt zu haben.

Münster, 09. Februar 2005

Christoph Baumann

